Nanosized Layered TOT Magnesium-Silicates: Equilibrium Morphologies and Surface Speciation, a Computational and Experimental Study

Hervé Toulhoat, Longfei Lin, Dalil Brouri, Jean-Marc Krafft, Yannick Millot, Guillaume Laugel, Hélène Lauron-Pernot

Nanosized Layered TOT Magnesium-Silicates: Equilibrium Morphologies and Surface Speciation, a Computational and Experimental Study

(Corrected version)

Hervé Toulhoat*, Longfei Lin †, Dalil Brouri, Jean-Marc Krafft, Yannick Millot, Guillaume Laugel, Hélène Lauron-Pernot

Sorbonne Université, CNRS, Laboratoire de Réactivité de Surface, F-75005, Paris, France

ABSTRACT

The morphology, surface speciation, NMR and IR spectroscopic properties of nanosized layered magnesium silicate isostructural to Talc at equilibrium in an aqueous environment were computed from first principles. The theoretical predictions were successfully compared with experimental results obtained on a commercial magnesium-silicate hydrate (MSH), revealing insight relevant for understanding the catalytic and other surface properties of such materials of promising industrial applications.

Introduction

  The prototype of layered magnesium silicates is natural Talc, a clay of large economic significance, with applications as filler for polymer composites, in cosmetics and human care products. In its pure form, Talc has unit formula $Si_4O_{10}Mg_3(OH)_2$ and crystallizes in space group N° 15 (C2/c). In this structure, presented on Figure 1, Mg^{2+} ions are six-fold coordinated by O^{2-} anions and arranged in planes of edge sharing octahedra, sandwiched between two planes of Si^{4+} centered corner sharing SiO_4 tetrahedra: these so-called TOT layers named phyllosilicates are stacked along the **c** axis, chemically independent but separated by a 0.284 nm van der Waals gap. Size of common commercial natural Talc particles is between 5 and 100 microns, and talc is considered as an hydrophobic non swelling clay mineral, expressing mostly the low surface energy {001} facets in its crystallites morphology, since cleavages along these planes requires only breaking non-covalent bonds in contrast to minority "edge" planes. However, the latter are expected to be hydrophilic and to offer more reactive surface species to chemical modifications or catalysis. Moreover, natural Talc may contain variable levels of impurities, mostly divalent cations such as Fe^{2+} substituted to Mg^{2+}. It is frequently associated with others mineral like chlorite, sulfurs, asbestos.

  Recently, various efforts achieved the synthesis of nanosized hydrated magnesium silicates, generically termed as MSH phases ([1]) that are often described as defectuous talcs([2]). Talc has significant industrial applications ([3]) but recently developed synthetic Nanotalcs present innovative surface properties for applications such as permeation barriers in polymer composites, emulsifiers

and viscosifiers in cosmetics formulae ([4],[5]). Applications of MSH in catalysis have been recently investigated by some of us ([6]). In this perspective, monitoring and controlling Talc nanoparticles morphologies and surface properties is crucial.

The present study was undertaken in order to help rationalizing the interpretation of structural and spectroscopic characterizations of MSH nanoparticles: starting from the experimental unit-cell of the bulk crystalline mineral, we have built atomistic stoichiometric slab models of Talc surfaces parallel to the Miller planes of lower indices, terminated according to chemical common sense so as to represent cleavages in a vacuum. These slab models were then reduced to include a single TOT layer amenable to full relaxation at the DFT/GGA/PAW/PBE level at a tractable cost of computer resources. Surface energies of these reference "dry" surfaces were determined according to the Methfessel-Fiorentini method ([7]) i.e. verifying the linearity between slab total energies and thicknesses for a given orientation. The influence of coverage by chemisorbed water on surface energies was then determined by adapting the methods developed by Digne et al. ([8]) and Arrouvel et al. ([9]) for γ-alumina and anatase surfaces respectively. The equilibrium morphologies and surface speciations of Talc as function of temperature and chemical potential of water were then determined according to the Gibbs-Curie-Wulff construction. Next, for each surface and coverage by water, normal modes of vibration and NMR parameters were computed by the linear response method at the proper DFT level of approximation ([10]). Finally, the most stable configurations for CO adsorption on the various surfaces were determined from simulations by a free energy analysis, and the corresponding Stark shifts of the adsorbed CO elongation mode of vibration extracted.

This ensemble of theoretical predictions was compared with good success to FTIR and MAS-NMR spectra recorded on a commercial MSH sample submitted to various pre-treatment protocols. Our results provide an insightful framework towards understanding and monitoring MSH and nanosized Talc surface properties.
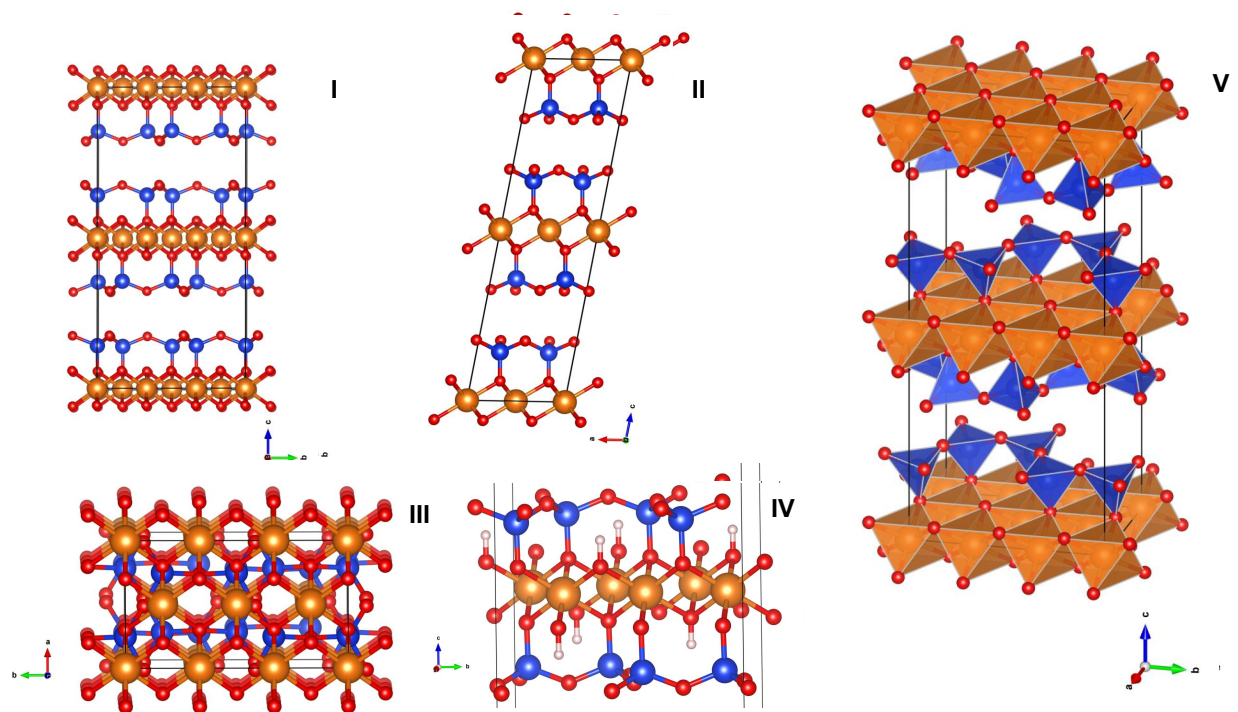
Figure 1: Unit-cell of Talc according to ([11]). Left panel, from left to right and top to bottom: ball and stick views along **a** (I), **b** (II) and **c** axis (III), and close-up of a TOT layer (IV) with DFT optimized positions of structural protons with Si^{4+} in blue, Mg^{2+} in orange, O^{2-} in red. H^+ in light grey; right panel, perspective view (V) evidencing MgO_6 octahedra (orange) and SiO_4 tetrahedra (blue). Structural hydrogens are not represented.

Theoretical Calculations

Construction of atomistic models

The bulk talc structure was recovered as file 9008040.cif ([11]) from the Crystallographic Open Database ([12]). Its unit-cell has stoichiometry of structural unit $Si_4O_{10}Mg_3(OH)_2$, multiplicity 4, symmetry C 2/c (space group 15) and lattice parameters a = 0.526 nm, b = 0.910 nm, c = 1.881 nm, alpha = 90.0°, beta = 100.0°, gamma = 90.0°. Bulk and surface models were built thanks to the MAPS interface (http://www.scienomics.com), which allowed moreover to conveniently prepare and submit DFT calculations, recover and analyze results. Since hydrogen positions are not detected by XRD, structural hydroxyls were first restored at their proper crystallographic sites in the bulk unit-cell, then a full structural relaxation of lattice parameters and atomic positions was performed. From the relaxed unit-cell were built oriented surface slab models of increasing thicknesses, with $\vec{c}$ axis parallel to the desired orientation {h, k, l} with respect to the original structure. Thicknesses were defined by a rank n, the integer number of structural units included, e.g. n= 4, 6, 8…, and an interslab gap of vacuum of 2 nm sufficient to minimize slab-slab interactions.

In order to obtain reference « bare », or zero coverage surface models, we choose to « prune » both {h, k, l}and {h, k, -l} surfaces symmetrically with the following chemical common sense criteria:

- Conserve stoichiometry, therefore electroneutrality, of the unit-cell.
- Simultaneously, maximize the coordination of terminal atoms.

In order to save CPU time, since a talc unit-cell comprises 2 identical chemically quasi-independent TOT layers interacting by dispersion forces only through a van der Waals gap (see

Figure 1), we choose to suppress one of them, keeping the same unit-cell in order to obtain a periodic model of an isolated TOT sheet.

Then, we built the precursors of rank n-1 or n-2 of surfaces of Highest Coverage (HC) by water by « pruning » again bare surfaces of rank n, to leave terminal cations with their full coordination spheres by O^{2-} in the bulk structure (e.g. Z = 6 for Mg^{2+}, Z = 4 for Si^{4+}). Further, we saturated terminal O anions with 1H (hydroxyl groups) or 2H (chemisorbed water), ending up with an integer number of adsorbate molecules (H_2O), and ensuring accordingly electroneutrality of the final HC slab.

We built surfaces of lower coverage by « pruning » water molecules, getting finally n.p slabs corresponding to initial conformations (p = number of coverages). In what follows, to represent the low coverage state (LC) we choose to remove each water molecule completing from Z = 5 to Z = 6 the coordination sphere of an edge Mg^{2+} ion, considering them as molecularly chemisorbed thus less strongly bonded than dissociatively chemisorbed water on edge Si^{4+}. We have therefore p = 2 (LC and HC).

Including the n reference "bare" surface models, we performed the DFT optimizations for the n.(p+1) models and obtained surface energies according to the Fiorentini-Methfessel method ([7]).

For the DFT simulation of CO adsorption, approximately symmetrical initial configurations were built including one CO molecule positioned in the vicinity of each surface site to be probed, on both sides of the slab model bearing this site.

DFT calculations

Total energy calculations were performed with the VASP version 5.4.1 software ([13]) within the density functional theory, using projected augmented wavefunctions, the PBE functional ([14]) in the

generalized gradient approximation and periodic boundary conditions. Atomic positions, and eventually unit-cell parameters, were optimized in order to minimize the total energy within the approximation chosen for the various atomistic models considered, taking advantage of symmetries. In all simulations, an energy cutoff of 400 eV was fixed for the planewave basis set. SCF cycles were converged to 10^{-4} eV, and ionic relaxation to 5.10^{-2} eVÅ^{-1}. Van der Waals corrections to the total energy were applied according to the zero damping DFT-D3 method of Grimme ([15]). Brillouin zone sampling was performed according to the automatic generation scheme implemented in VASP or limited to the gamma point for the larger unit-cells. Hessian matrices and NMR chemical shifts tensors were computed for previously relaxed models according to the linear response method ([16, 10]). Normal mode frequencies in the harmonic approximation were computed from the Hessian matrices for comparison with absorption bands recorded in experimental FTIR spectra. Anharmonicity constants $\omega_e \chi_e$ to correct the $\nu(O-H)$ stretching modes of the various hydroxyls groups were not calculated from first principles but rather deduced by comparison with known assignments so that the corrected fundamental stretching frequencies ω_{01} were deduced from the calculated harmonic frequencies ω_e according to $\omega_{01} = \omega_e - 2\omega_e \chi_e$. Isotropic chemical shifts δ for ^{1}H, ^{29}Si, and ^{25}Mg nuclei were predicted from calculated on site shielding constants σ using the linear correlations obtained with respect to experimental references. The details of these calibrations can be found in Supporting Information. Calculated absolute isotropic shielding constants for valence and core electrons were systematically considered for these calibrations.

Determination of surface energies

For the determination of orientation dependent surface energies, we have followed the approximations detailed in ([8]) and ([17]):

For the "bare" reference surfaces we used equation (1) to compute surface energies Γ_{hkl}^0:

$$\Gamma_{hkl}^0 = \frac{[G(surf\ hkl) - G(bulk)]}{A_{hkl}} \approx \frac{[E_{0K}(surf\ hkl) - E_{0K}(bulk)] - T[S_{vib}(surf\ hkl) - S_{vib}(bulk)]}{A_{hkl}} \qquad (1)$$

With $G(surf\ hkl)$ the free energy per unit-cell of a slab model of the { h, k, l } surface, $G(bulk)$ the free energy per unit-cell of bulk solid including the same number of stoichiometric units as in the slab model, and A_{hkl} the total area at the slab-vacuum interface (twice the slab section normal to the slab $\vec{c}$ axis. $E_{0K}(surf\ hkl)$ and $E_{0K}(bulk)$ stand for the DFT total energies of the relaxed corresponding models, approximating the free energies. $S_{vib}(surf\ hkl)$ and $S_{vib}(bulk)$ stand for the vibrational entropies at T Kelvin computed from the list of normal mode frequencies computed for the corresponding models.

Similarly, adsorption energies per water molecule at water coverage Θ_{hkl} of n water molecules per unit area of (h, k, l) surface are approximated by:

$$E_{hkl}^{ads} = \frac{[E(surf\ hkl + nH_2O) - E(surf\ hkl)]}{n} - E(H_2O) \qquad (2)$$

$$E_{hkl}^{ads} \approx \frac{[E_{0K}(surf\ hkl + nH_2O) - E_{0K}(bulk)]}{n} - E_{0K}(H_2O) \qquad (3)$$

Where $E_{0K}(surf\ hkl + nH_2O)$ and $E_{0K}(bulk)$ stand for the DFT total energies of the slab model covered by n water molecules and of the bulk unit-cell respectively, while $E_{0K}(H_2O)$ stands for the DFT total energy of a single water molecule.

9

Applying the Gibbs theorem of adsorption, the surface energies as function of the chemical potential of water, taking into account vibrational entropy of adsorbed water are finally computed according to:

$$\Gamma_{hkl} = \Gamma_{hkl}^0 + \Theta_{hkl}\left(E_{hkl}^{ads} - T\frac{[S_{vib}(surf\ hkl+nH_2O)-S_{vib}(surf\ hkl)]}{n} - \Delta\mu(H_2O)\right) \qquad (4)$$

With:

$$\Delta\mu(H_2O) = h_{H2O}^0(T) - Ts_{H2O}^0(T) + RTLn\left(\frac{P_{H2O}}{P_{H2O}^0}\right) - E_{0K}(H_2O) \qquad (5)$$

And:

$$\Theta_{hkl} = \frac{n}{A_{hkl}} \qquad (6)$$

Where $h_{H2O}^0(T)$ and $s_{H2O}^0(T)$ are the enthalpies and entropies of water at T referred to their values at the standard state, $P_{H2O}^0 = 1\ bar$ is the standard pressure, and P_{H2O} the partial pressure of water imposed above the surface. For the thermodynamic properties of water we used the polynomial expansions in the range 500-1700K (Shomate equations) as available from the NIST database (https://webbook.nist.gov) [18].

Determination of equilibrium morphologies

Equilibrium morphologies were obtained according to the Gibbs-Curie-Wulff construction, following:

$$\frac{\Gamma_{hkl}}{d_{hkl}} = \alpha\ \forall\ h,k,l \qquad (7)$$

Where d_{hkl} is the distance of face (hkl) from the origin, α a scale factor, and Γ_{hkl} the surface energy computed as indicated in the previous section. Polyhedra representative of the predicted morphologies were built thanks to the VESTA software [19].

Simulation of CO adsorption

Physisorbed CO is responsive to the local electric field gradient by blue or red shifts of its stretching frequency detectable in the IR range (vibrational Stark effect ([20])). We have probed various sites on our model surfaces by looking for the local minimum of van der Waals corrected total energy for slabs plus two adduct molecules of CO placed on both symmetrical vacuum/slab interfaces. Normal modes frequencies for the geometry optimized configuration were then calculated, providing both entropic corrections to CO adsorption energies and vibrational Stark shifts for comparison with experiments. Free energies of CO adsorption at some surface site and temperature T, $\Delta G_{ads}(CO@S, T)$, were evaluated according to:

$$\Delta G_{ads}(CO@S, T) = \left[G_{vib}(CO@S,T) + \frac{2G_{trans+rot}\left(CO_g(P,T)\right)}{3} - \left(G_{vib}(S,T) + 2G_{tot}\left(CO_g(P,T)\right) \right) + 2\Delta E_{ads}(CO@S) \right]/2 \qquad (8)$$

Where $G_{vib}(CO@S,T)$ is the vibrational contribution to the free energy of the surface model + 2 CO adducts, $G_{vib}(S,T)$ the vibrational contribution to the free energy of the surface model without CO adducts, $G_{tot}\left(CO_g(P,T)\right)$ the total free energy of CO at pressure P and temperature T computed ab initio (at the 6-31G* level and functional B3LYP), and $\Delta E_{ads}(CO@S)$ the change of total energy of the surface slab model upon adsorption of one CO adduct. The term $\frac{2G_{trans+rot}\left(CO_g(P,T)\right)}{3}$ accounts for the residual degrees of freedom of the 2 CO adducts, assumed to be able to rotate around their principal axis and translate parallel to a surface.

The value calculated according to equation (8) is significantly dependent on the size of the slab model, and the quality of geometry optimizations. Indeed, calculated vibrational entropies are very sensitive to the number and accuracy of "soft" modes (low frequencies) taken into account. In view of the very large computer time invested in these vibrational calculations, we limited the slab sizes

to 3 stochiometric units, and could not avoid the appearance of some low frequency imaginary modes indicative that the geometry was not fully converged. However, considering that the model substrate with and without adducts differ essentially by the surface groups and must have "bulk" phonons in common, we choose to retain in the calculation only modes with wavenumbers above 1000 cm^{-1}, representative of surface phonons.

Experimental Methods

MSH sample

Magnesol® catasorb was kindly provided by the Dallas group of America©. It contains Cl (<0.5%) and Na (<2%) impurities. The results for this material will be displayed as MSH "com" for commercial. Experimental XRD pattern, SEM, NMR and DRIFTS characterizations of this material have been already published by our group ([6], [21]). The specific surface area was calculated from the BET equation and is 421 $m^2.g^{-1}$.The bulk Mg/Si molar ratio measured by X-Ray Fluorescence (XRF) for MSH com is 0.290, while it is 0.485 in surface as measured by X-ray Photoelectron spectroscopy (XPS).

FTIR

FTIR spectra of adsorbed CO were collected on a Bruker Vertex 70 spectrometer using a MCT detector (resolution 2 cm^{-1}, 64 scans per spectrum). The assembly is consisting of three parts: evacuation and gas system, IR measuring cell, and the spectrometer. The IR measuring cell allows one to raise or lower the sample vertically between the two sections of the cell: the upper oven section in which thermal treatment takes place and the lower section equipped with a perpendicular

body mounted with CaF_2 windows, cooled to liquid nitrogen temperature, where measurements are made. The sample was pressed into self-supported wafers of 21.1 mg, diameter 16 mm. The wafer was first heated in situ at 70, 90, 140 and 350 °C, respectively, for 2 h under a flow of Ar (20 $cm^3.min^{-1}$), before being evacuated (5 x 10^{-6} Torr) for 1 h. The wafer was then moved to the lower part of the cell, which was cooled down to temperature of liquid nitrogen. CO pulses were successively added up to an equilibrium pressure of 133 Pa. After introduction of CO a FTIR spectra was recorded at an equilibrium pressure of 10 Pa. Then FTIR spectra were recorded every two minutes during evacuation (up to 5.10^{-4} Pa). The difference spectra were obtained by subtracting the spectra of the pretreated sample (before increments of CO) recorded at the liquid nitrogen temperature from those recorded after successive increments of CO.

ELECTRON MICROSCOPY

Scanning electron microscopy (SEM) with field emission gun images were recorded with a Hitachi SU-70 field emission gun scanning electron microscope. The samples were fixed on an alumina SEM support with carbon adhesive tape and were observed without metallization. The accelerating voltage was 1 kV, and the working distance was around 4 mm.

Transmission electron microscopy (TEM) was carried out on Jeol 2011 LaB6 microscope, operating at 200 kV equipped with a 4 K camera (Orius Gatan) for micrograph acquisition. For TEM observations, the samples were ultrasonically dispersed in ethanol and a drop is then deposited and dried on carbon coated copper grid.

Results

Influence of water adsorption on surface energies and equilibrium morphologies

Parker et al. have recently studied the interactions of pyrophyllite edge surfaces with water[22] by means of DFT and forcefield simulations. Since pyrophyllite of formula $Si_4O_{10}Al_2(OH)_2$ is the analog TOT Aluminum-silicate of the magnesium-silicate considered in the present report, we considered similar edge orientations as these authors, namely {-110}, {010}, {130}, {100}, and the basal plane {001}.

The {001} orientation required a specific approach: by difference between DFT energies of a relaxed periodic model representing an interface between bulk water and bulk talc, and the sum ot totl energis of the relaxed periodic model of the interface without water and a periodic model of bulk water, we obtain an approximation of the work of adhesion of bulk water to the bare {001} external surface, minus the surface energy of bulk water: $\left(W_{adh,001}^{W} - \gamma_{LG}\right) = 0.103\,\boldsymbol{J.m^{-2}}$

The surface energy of the bare {001} surface is half the energy required to cleave the crystal amid the van der Waals gap between two consecutive TOT layers. We approached this quantity by difference between DFT energies of the relaxed periodic model of bulk talc and twice that of a relaxed model of bulk talc with one over two TOT layers removed. The value we obtain is $\boldsymbol{\Gamma_{001}^{0}} = 0.064\,\boldsymbol{J.m^{-2}}$.

We needed then to evaluate the spreading pressure[25] $\Pi_{001}\left(T, \frac{P_{H2O}}{P_{H2O}^0}\right)$, i.e. the difference between $\boldsymbol{\Gamma_{001}^{0}}$ and $\Gamma_{001}\left(T, \frac{P_{H2O}}{P_{H2O}^0}\right)$, the surface energy of the {001} surface in equilibrium with water at temperature T and relative partial pressure of water $\frac{P_{H2O}}{P_{H2O}^0}$. This term is provided by equation (4):

$$\Gamma_{hkl} = \Gamma_{hkl}^0 + \Theta_{hkl}\left(E_{hkl}^{ads} - T\frac{[S_{vib}(surf\ hkl + nH_2O) - S_{vib}(surf\ hkl)]}{n} - \Delta\mu(H_2O)\right)$$

So that:

$$\Pi_{001}\left(T,\frac{P_{H2O}}{P_{H2O}^0}\right) = \Gamma_{001}^0 - \Gamma_{001}\left(T,\frac{P_{H2O}}{P_{H2O}^0}\right) \tag{9}$$

Therefore:

$$\Pi_{hkl}\left(T,\frac{P_{H2O}}{P_{H2O}^0}\right) = -\Theta_{hkl}\left(E_{hkl}^{ads} - T\frac{[S_{vib}(surf\ hkl + nH_2O) - S_{vib}(surf\ hkl)]}{n} - \Delta\mu(H_2O)\right) \tag{10}$$

In equation (8), the term accounting for the difference of vibrational entropy between the hydrated and bare surfaces cancels out since physisorbed water molecules are not bound to surface sites. However, we considered similarly as in (8) that the entropy change upon adsorption of weakly bounded water is about 1/3 of the gas phase entropy [26, 27]. Equation (9) becomes then for the {001} surface and water:

$$\Pi_{001}\left(T,\frac{P_{H2O}}{P_{H2O}^0}\right) \approx -\Theta_{001}^W\left(\boldsymbol{E_{001}^{ads,W}} - h_{H2O}^0(T) + \frac{Ts_{H2O}^0(T)}{3} - RTLn\left(\frac{P_{H2O}}{P_{H2O}^0}\right) + E_{0K}(H_2O)\right) \tag{11}$$

The physisorption energy of water was estimated to correspond to 2 hydrogen bonds, and evaluated by DFT as one half the energy of vaporization of bulk water, i.e 1/N the difference between the total energy of a relaxed cubic periodic model of N molecules of bulk water (i.e. of concentration 55.5 mol.L^{-1}) and N times that of a cubic periodic model of the same size containing an isolated water molecule. Following this procedure, the value $\boldsymbol{E_{001}^{ads,W}} = -30.3\ kJ.mol^{-1}$ we obtain is consistent with the experimental estimate reported in[4]. Estimating the equilibrium coverage Θ_{001}^W by physisorbed water by DFT simulation was out of reach since it would imply long ab initio molecular dynamics and a very large unit-cell. Rather, we fixed this coverage so as to match the average experimental contact angle $\theta_W = 80.4\,°$ of liquid water on talc at ambient

temperature[28], which measured on compressed sedimented powder mostly reflects the {001} surface wettability thus $\theta_{W,001}$

For that purpose, we apply the Young equation that becomes with our notations:

$$\Gamma_{001}\left(300K, \frac{P_{H2O}}{P_{H2O}^0} = 1\right) - \mathbf{\Gamma_{001}^W} - \gamma_{LG}\cos\theta_{W,001} = 0 \tag{12}$$

Where $\gamma_{LG} = 0.072 \, \boldsymbol{J.m^{-2}}$ is he surface tension of liquid water at 300 K.

The expression of $W_{adh,001}^W$:

$$W_{adh,001}^W = \mathbf{\Gamma_{001}^0} + \gamma_{LG} - \mathbf{\Gamma_{001}^W} \tag{13}$$

gives an approximation of $\mathbf{\Gamma_{001}^W}$:

$$\mathbf{\Gamma_{001}^W}\left(300 \, K, \frac{P_{H2O}}{P_{H2O}^0} = 1\right) \approx \mathbf{\Gamma_{001}^0} + \gamma_{LG} - W_{adh,001}^W \approx -0.039 \, \boldsymbol{J.m^{-2}} \tag{14}$$

Combining (9) and (11), the Young equation becomes:

$$\left(\mathbf{\Gamma_{001}^0} - \Pi_{001}\left(300K, \frac{P_{H2O}}{P_{H2O}^0} = 1\right) - \mathbf{\Gamma_{001}^W}\left(300 \, K, \frac{P_{H2O}}{P_{H2O}^0} = 1\right)\right) = \left(\cos\theta_{W,001}\right)\gamma_{LG} \tag{15}$$

Solving (15) for $\theta_{W,001} = 80.4°$ we obtain $\Theta_{001}^W = 3.5 \, molec \, H_2O.nm^{-2} = 5.8 \, \mu mol.m^{-2}$, or

$1.69 \, molec \, H_2O/48.19 \, Å^2$, while equation (9) results in $\Gamma_{001}\left(300 \, K, \frac{P_{H2O}}{P_{H2O}^0} = 1\right) =$

$-0.027 \, J.m^{-2}$.

Interestingly, both surface energies $\mathbf{\Gamma_{001}^W}$ and $\Gamma_{001}\left(300 \, K, \frac{P_{H2O}}{P_{H2O}^0} = 1\right)$ appear as slightly negative,

therefore vapor and liquid covered parts of the {001} surface tend to expand: they compete to repel

the triple line, which is equilibrated by the force $\left(\cos\theta_{W,001}\right)\gamma_{LG}$ tending to contract the liquid-

vapor interface. This explains the partial wetting of talc by liquid water in ambient conditions.

Our results are summarized in Table 1.

Table 1: Comparison of DFT results obtained for various orientations of magnesium-silicate TOT minerals. Γ_{hkl}^0 : surface energy of the bare surface ; Θ_{hkl}^{LC} : lower coverage by dissociatively chemisorbed water, product of Si-O-Si edge bridges hydrolysis ; Θ_{hkl}^{HC} : higher coverage, i.e. Θ_{hkl}^{LC} augmented by molecularly chemisorbed water on coordinatively unsaturated edge Mg sites ; $E_{hkl}^{ads,LC}$ $(kJ.mol^{-1})$: average chemisorption energy of water at low coverage ; $E_{hkl}^{ads,HC}$ $(kJ.mol^{-1})$: average chemisorption energy of water at high coverage ; $E_{hkl}^{ads,H_2O@Mg}$: average energy of molecular chemisorption of water on coordinatively unsaturated edge Mg sites ; A_{hkl} : area at the slab-vacuum interface.

{hkl}	-110	010	130	100	001
Γ_{hkl}^0 $(J.m^{-2})$	2.47	2.32	1.12	1.40	0.064
Θ_{hkl}^{LC} $(H_2O/TOT\ edge)$	4	1.5	4	2	1.69
Θ_{hkl}^{HC} $(H_2O/TOT\ edge)$	8	3.5	10	5	0
$E_{hkl}^{ads,LC}$ $(kJ.mol^{-1})$	-289.2	-470.3	-264.3	-327.7	-30.3
$E_{hkl}^{ads,HC}$ $(kJ.mol^{-1})$	-198.0	-260.9	-155.9	-182.6	-
$E_{hkl}^{ads,H_2O@Mg}$ $(kJ.mol^{-1})$	-106.9	-103.8	-83.7	-85.7	-
A_{hkl} $(Å^2)$	196.97	97.44	338.75	171.17	48.19

From Table 1, first line, it is already clear that bare edges {-110} and {010} are energetically disfavoured compared to bare edges {130}, {100} and of course the basal plane {001}. Water adsorption does reduce surface energies, as expected, as shown on Figure 2:
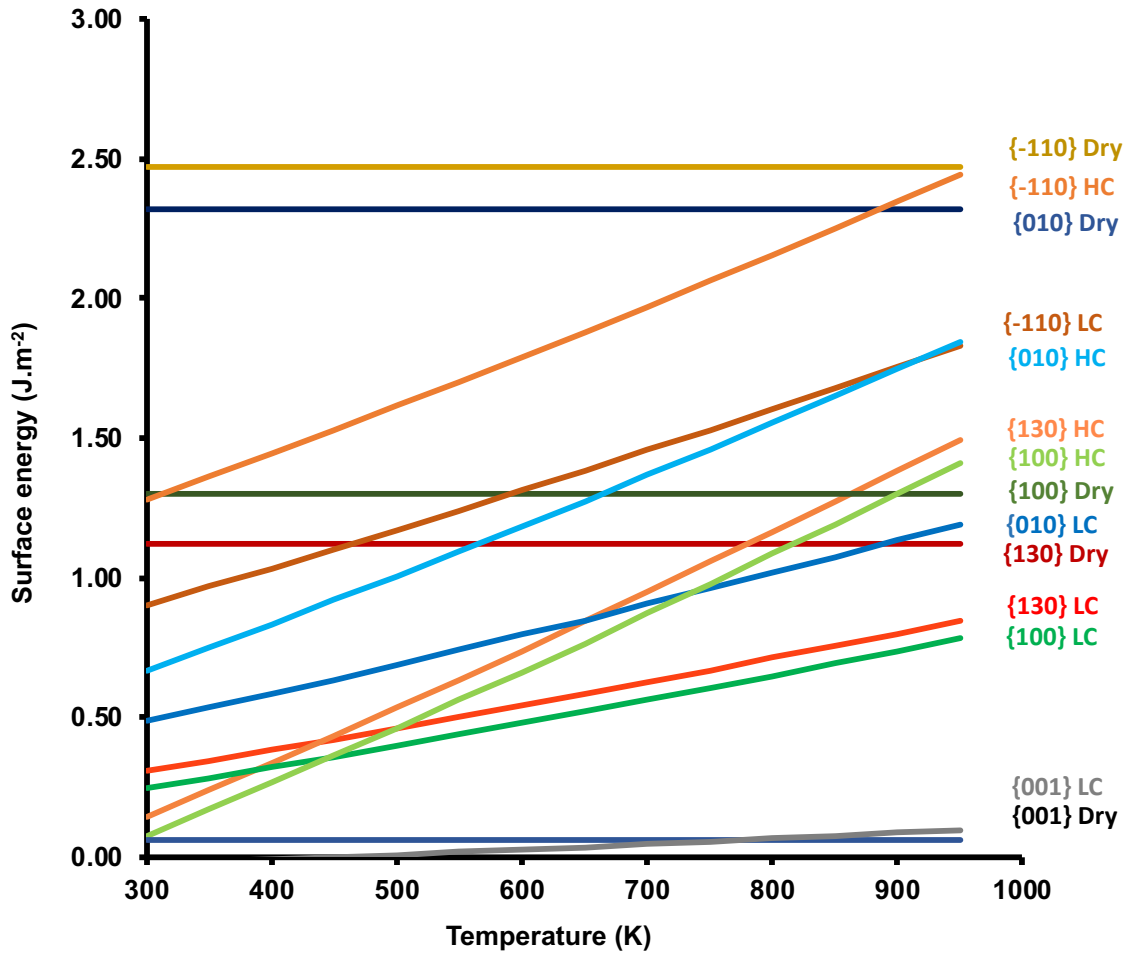
Figure 2: Influence of temperature on TOT magnesium-silicates edges surface energies in presence of saturated water vapor. Dry label stands for zero coverage by water, LC for low coverage by water and HC stands for high coverage by water. Hydrated edges {130}, {100} have surface energies about 1 J.m^{-2} lower than hydrated {-110} and {010} edges. Hydrophobic {001} basal planes have a much lower surface energy since they are created by cleavage between weakly interacting TOT layers. Entropic vibrational terms are neglected in a first approximation of surface energies

The morphology at 600K and $\frac{P_{H2O}}{P_{H2O}^0} = 1$, is representative of usual hydrothermal synthesis conditions. We have obtained $\Gamma_{130}\left(600\,K, \frac{P_{H2O}}{P_{H2O}^0} = 1\right) = 0.320\,J.m^{-2}$., $\Gamma_{100}\left(600\,K, \frac{P_{H2O}}{P_{H2O}^0} = 1\right) = 0.270\,J.m^{-2}$., and $\Gamma_{001}\left(600\,K, \frac{P_{H2O}}{P_{H2O}^0} = 1\right) = 0.026\,J.m^{-2}$.

The Gibbs-Curie-Wulff construction of the equilibrium morphology at 600K and saturated water vapor excludes {-110} and {010} edges, as shown in Table 2.

Including vibrational entropic contributions to surface free energies for the selected edges allowed also more precise determinations of transition temperatures between high and low coverages by water at a given relative humidity, as presented on Figure 3 and 4. These transition temperatures are sensitive to the edge orientation and relative humidity, being shifted down by 111.3 K and 171.2 K for {130} and {100} edges respectively, when the ratio $\frac{P_{H2O}}{P_{H2O}^0}$ decreases from 1 to 0.01. The onset of low coverage (desorption of molecular water) occurs above very similar temperatures (~ 513 K) for both edges at the lower relative humidity. It is rather different at saturating vapor pressure of water, ~ 627K and ~ 687 K for {130} and {100} respectively, in agreement with the slightly more negative adsorption energy of molecular water at edge Mg sites (Table 1, line 6). The slight stabilization of {130} and {100} edges with respect to the {001} basal facets induced by vibrational entropy of chemisorbed water has some effect on the equilibrium morphology as can be deduced from the comparison of fractional areas in Table 2. A representation of the equilibrium morphology corresponding is shown on Figure 5.

Table 2: Morphology of a hydrated TOT magnesium-silicate at 600K and $P_{H_2O}/P_{H_2O}^0 = 1$. D_{hkl} is the distance of face (hkl) from the origin, proportional to Γ_{hkl} , equation (7), computed at these conditions without/with vibrational entropic corrections. The arbitrary scale factor $\alpha = 10^{-21}$ J.Å^{-1} was chosen for optimal visualization of the morphology through the VESTA program in comparison to the unit-cell dimensions, see Figure 5.

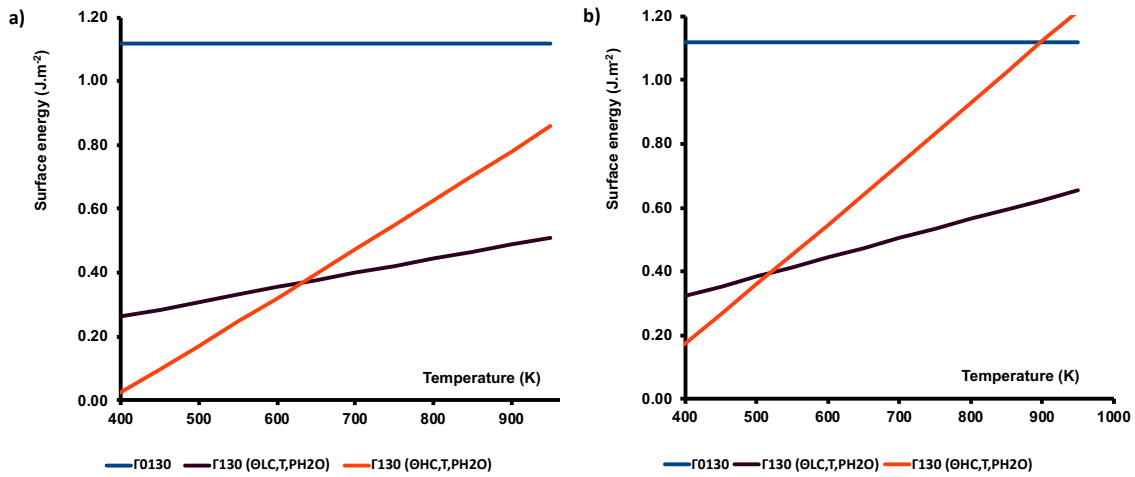| {khl}	D_{hkl} (Å)	Area (Å^2)	% of total area
001	0.26/0.26	95.04/32	90.38/85.2
00-1	0.26/0.26	95.04/32	
-110			0
1-10			
110			
-1-10			
010			0
0-10			
130	5.42/3.2	2.94/1.65	5.62/8.79
-1-30	5.42/3.2	2.94/1.65	
-130	5.42/3.2	2.94/1.65	
1-30	5.42/3.2	2.94/1.65	
100	4.82/2.7	3.66/2.25	3.50/5.98
-100	4.82/2.7	3.66/2.25	

Figure 3: Influence of temperature on TOT magnesium-silicates {130} edges surface energies in presence of a) saturated water vapor, i.e. $\frac{P_{H2O}}{P_{H2O}^0} = 1$; b) $\frac{P_{H2O}}{P_{H2O}^0} = 0.01$. Θ_{LC} stands for low coverage by water, and Θ_{HC} stands for high coverage by water. The transition temperature above which low coverage is more stable than high coverage, decreases from 626.6 K in the a) case to 515.3 K in the b) case. Vibrational corrections to surface free energies are included in the calculations.
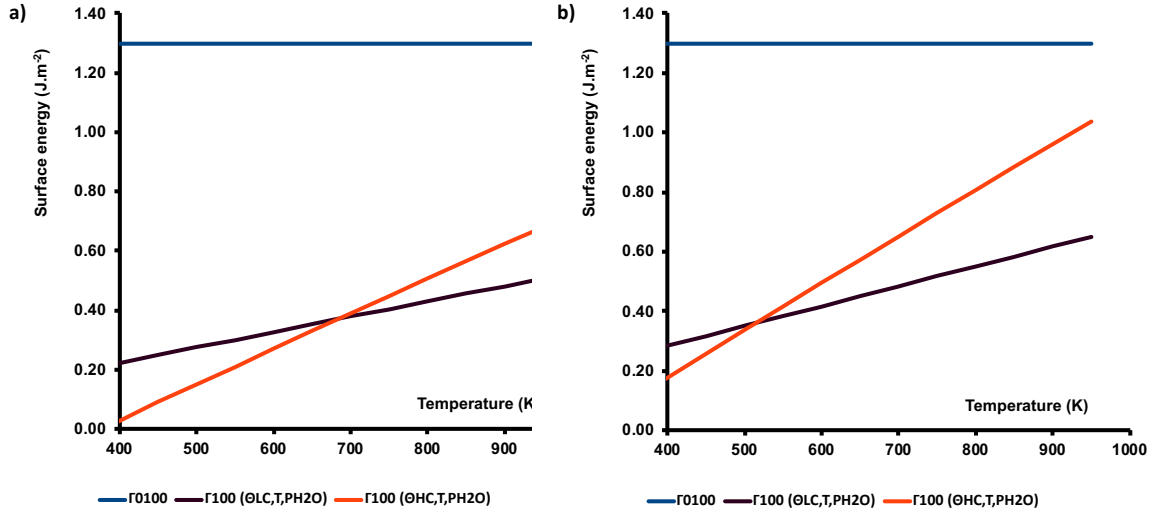
Figure 4: Influence of temperature on TOT magnesium-silicates {100} edges surface energies in presence of a) saturated water vapor, i.e. $\frac{P_{H2O}}{P_{H2O}^0} = 1$; b) $\frac{P_{H2O}}{P_{H2O}^0} = 0.01$. Θ_{LC} stands for low coverage by water, and Θ_{HC} stands for high coverage by water. The transition temperature above which low coverage is more stable than high coverage, decreases from 686.6 K in the a) case to 515.4 K in the b) case. Vibrational corrections to surface free energies are included in the calculations.
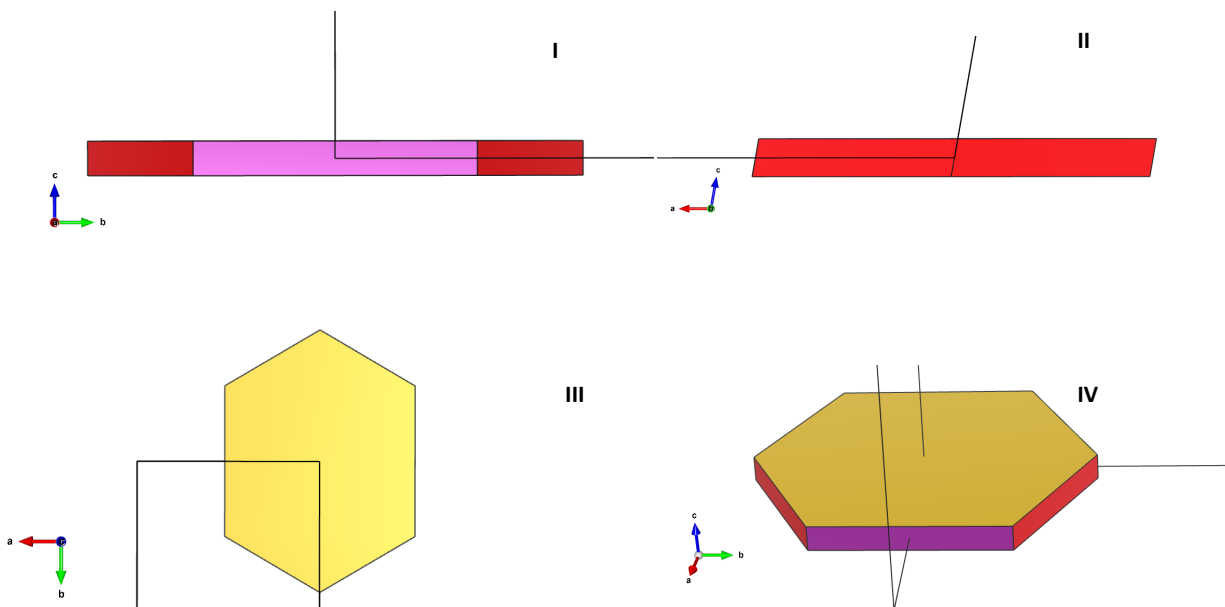
Figure 5: Representation of predicted nanotalc equilibrium morphology at 600K and $P_{H_2O}/P_{H_2O}^0 = 1$ including vibrational corrections. From left to right and top to bottom: view along **a** axis (I), **b** axis (II), **c** axis (III), and perspective view (IV). Black lines delimit unit-cell. Orange: 2 {001} facets; red 4 {130} facets; magenta 2 {100} facets.

Comparison of predicted and experimental infra-red spectra of surface species

DRIFTS

Figures 6 a), b) and c) represent the conformations of minimal total energy for the slab models of the {130} surface at zero, low and high water coverages respectively, while Figure 7 a), b) and c) are similar for the {100} surface.

The calculated normal modes of vibration in the wavenumber range 1500-4000 cm⁻¹ and their assignation are presented in Table S1 in Supporting Information. These modes correspond to the elongation and bending of O-H bonds for the various situations encountered in these models: bulk and surface "structural" hydroxyls, surface silanols, and molecularly chemisorbed water. As introduced in the DFT calculations section above, anharmonicity corrections were applied to

hydroxyls elongation modes. They were estimated by matching experimental and calculated average wavenumbers to be $\omega_e \chi_e = 36.7\ cm^{-1}$ and $\omega_e \chi_e = 57.4\ cm^{-1}$ for edge Si-OH and structural Mg-OH groups respectively. Figures 8a) and b) show experimental DRIFTS spectra (continuous lines) obtained for MSH com taken at 343K after a pretreatment one hour under argon flow at 343K and at 413K after a pretreatment one hour under argon flow at 623K. A transition from HC to LC should thus be observed as the pretreatment temperature increases above 515.4 K. Calculated lines are superimposed on these spectra, including predicted modes for {130} (red) and {100} (green) edges at high coverage (8a) and low coverage by water (8b).

For low temperature pretreatment, the experiment reveals broad bands in the 3000-3700 cm^{-1} and 1600-1700 cm^{-1} ranges assigned to stretching and bending modes of adsorbed water respectively, plus sharper lines peaking at 3672 and 1630 cm^{-1} assigned in the literature to the stretching mode of internal (structural) hydroxyl groups and a bending mode of molecularly adsorbed water respectively. The calculated lines match experiments rather well. Stretching modes of hydroxyl linked to surface Mg ions in the {130} model, predicted to vibrate around 4000 cm^{-1} do not appear however in the experimental spectra.

After pretreatment, the band in the 1600-1700 cm^{-1} have almost disappeared, as well as the peak at 1630 cm^{-1}, a clear indication of desorption of molecular water, as predicted by our calculations to be the case above 515.4 K under dry atmosphere. (Figures 3 and 4). Conversely, sharp peaks now emerge at 3730 cm^{-1}, which can be assigned by comparison to our calculations and reference to literature to the stretching modes of edge silanols.

Anharmonicity corrections mentioned above have been applied to the corresponding calculated lines shown on Figures 8a) and 8b).
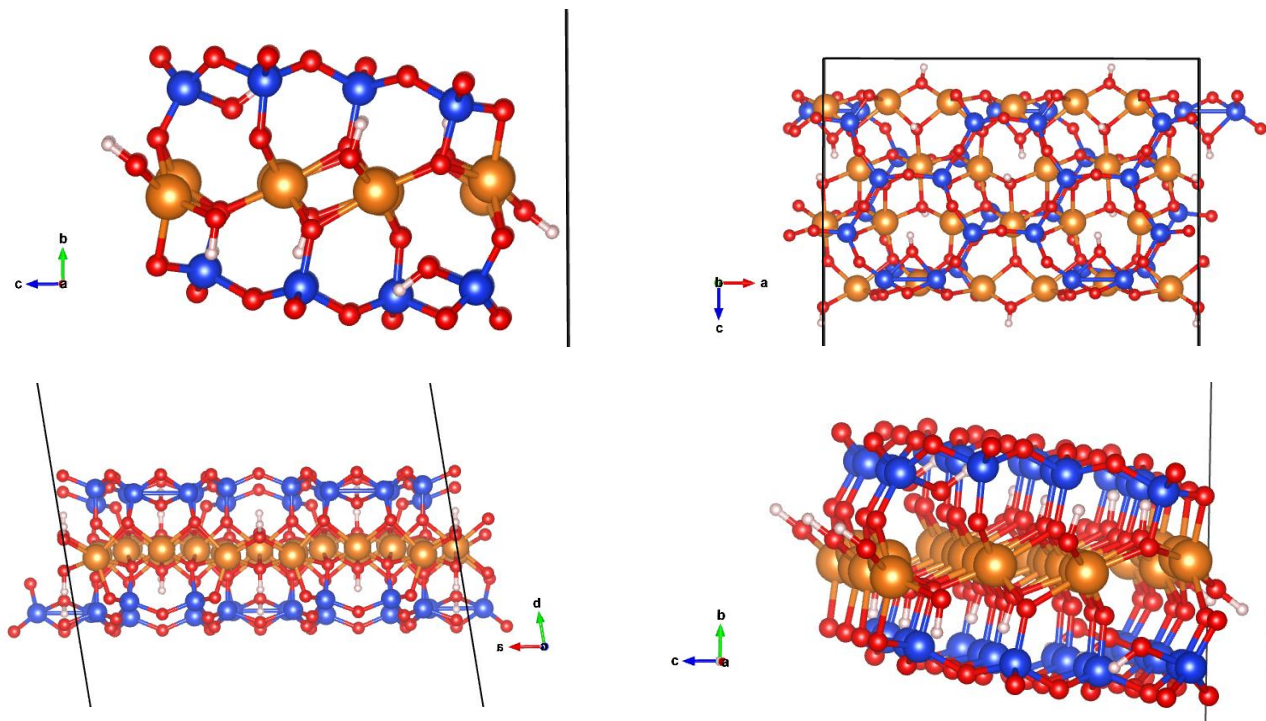
Figure 6a: Geometry optimized slab model of the {130} surface at zero coverage by water: from top left to bottom right, views along -a, -c, -b axis and perspective view. 3 structural Mg-OH groups emerge per edge face.
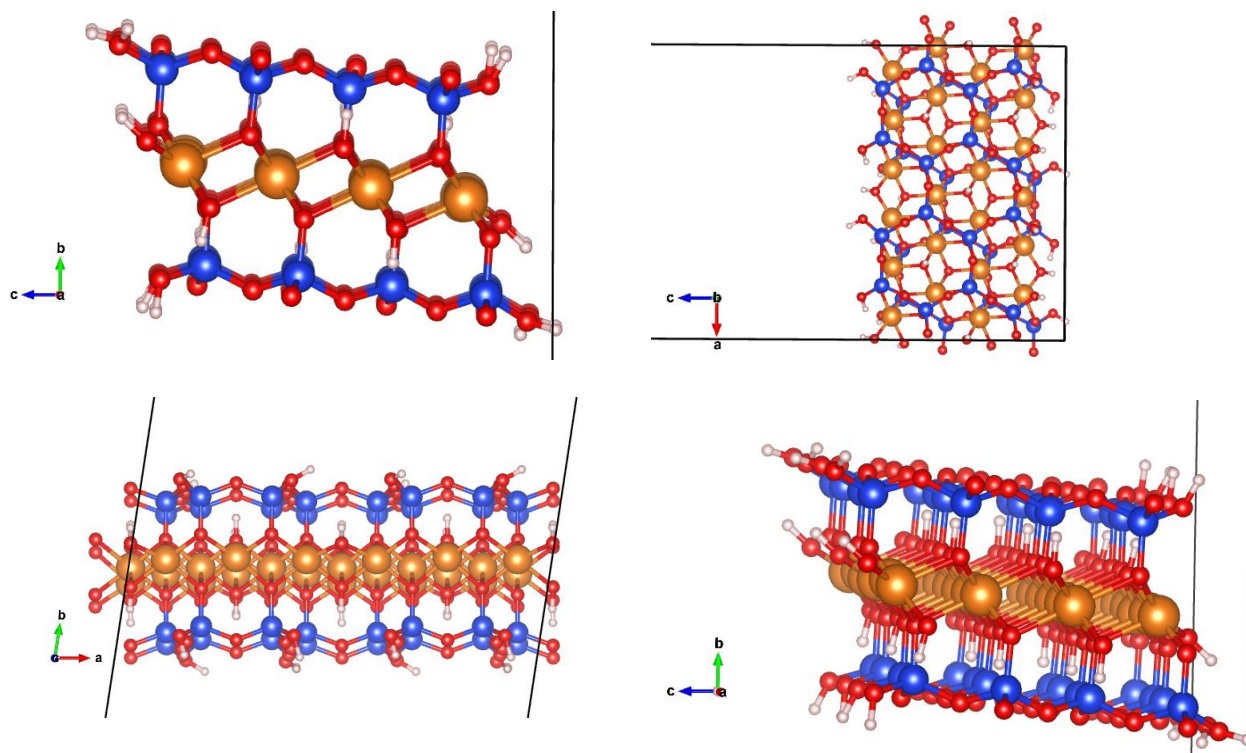
Figure 6b: Geometry optimized slab model of the {130} surface at low coverage by water (4 H$_2$O per face, dissociated to give 8 edge Si-OH): from top left to bottom right, views along -a, -c, -b axis and perspective view.
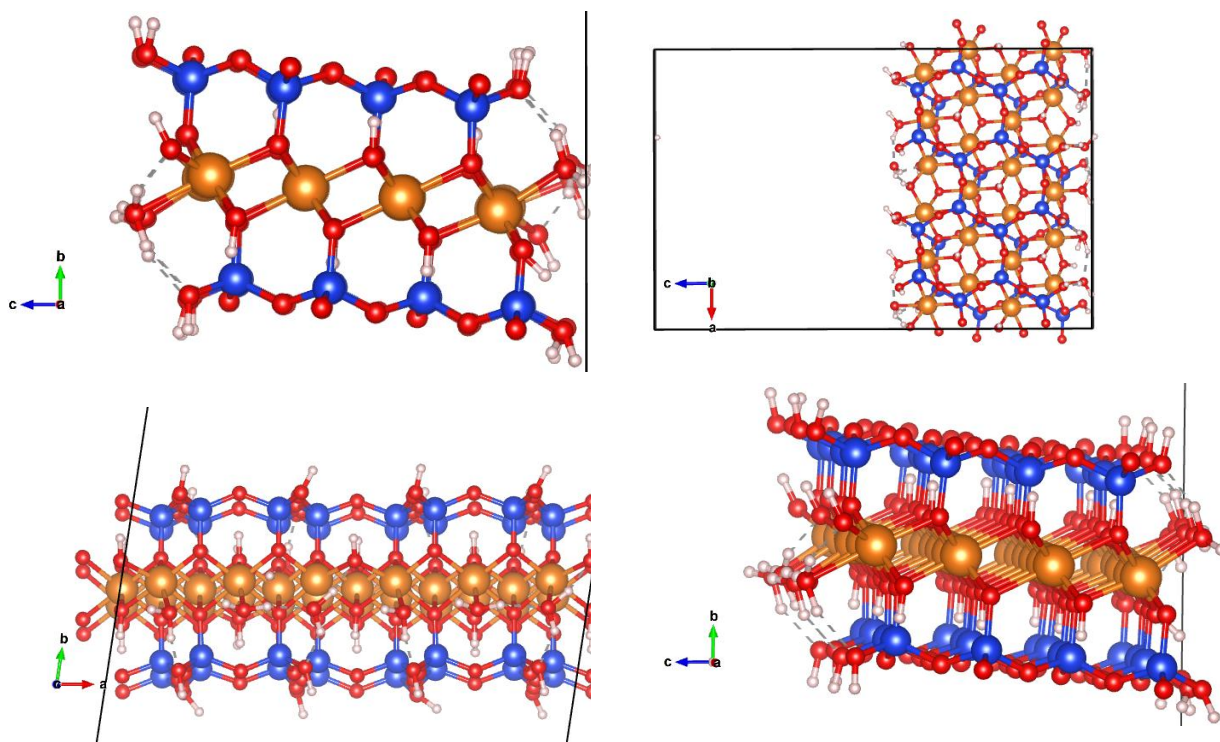
Figure 6c: Geometry optimized slab model of the {130} surface at high coverage by water (10 H_2O per face, 4 dissociated to give 8 edge Si-OH, 6 molecularly chemisorbed on edge Mg ions): from top left to bottom right, views along -a, -c, -b axis and perspective view.
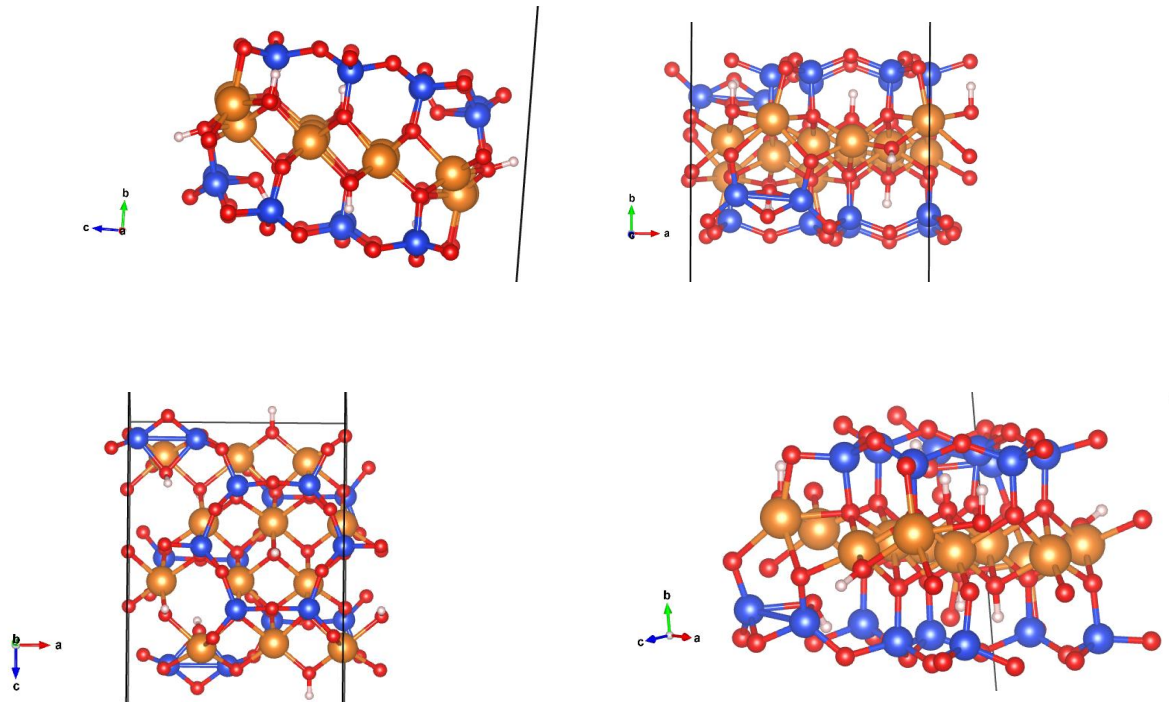
Figure 7a: Geometry optimized slab model of the {100} surface at zero coverage by water: from top left to bottom right, views along -a, -c, -b axis and perspective view. One structural Mg-OH group emerge per edge face
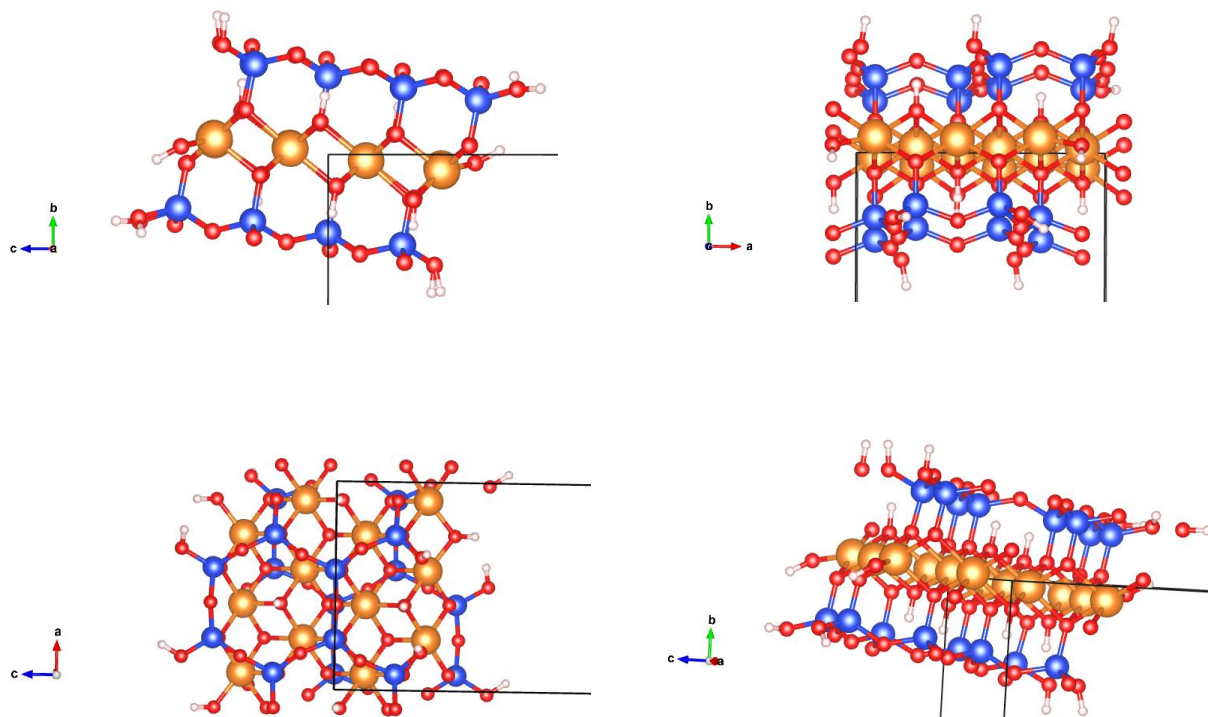
Figure 7b: Geometry optimized slab model of the {100} surface at low coverage by water (2 H_2O per face, dissociated to give 4 edge Si-OH): from top left to bottom right, views along -a, -c, -b axis and perspective view.
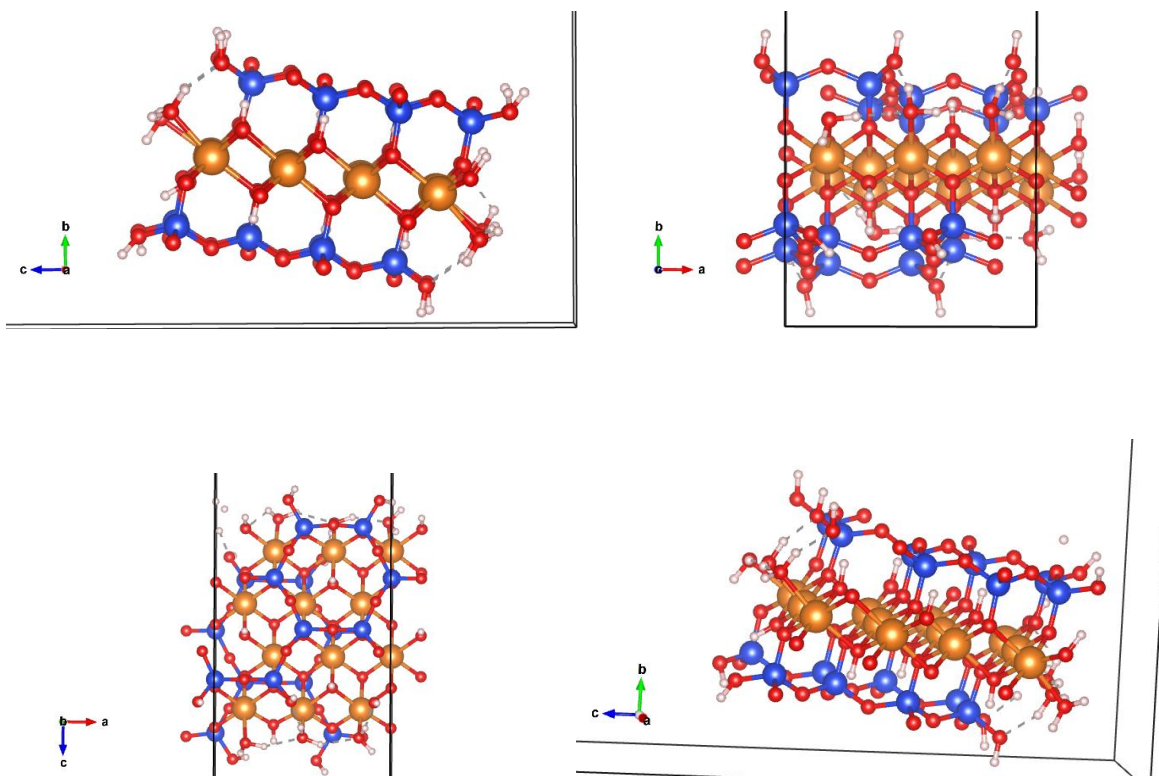
Figure 7c: Geometry optimized slab model of the {100} surface at high coverage by water (5 H_2O per face, 2 dissociated to give 4 edge Si-OH, 3 molecularly chemisorbed on edge Mg ions): from top left to bottom right, views along -a, -c, -b axis and perspective view.
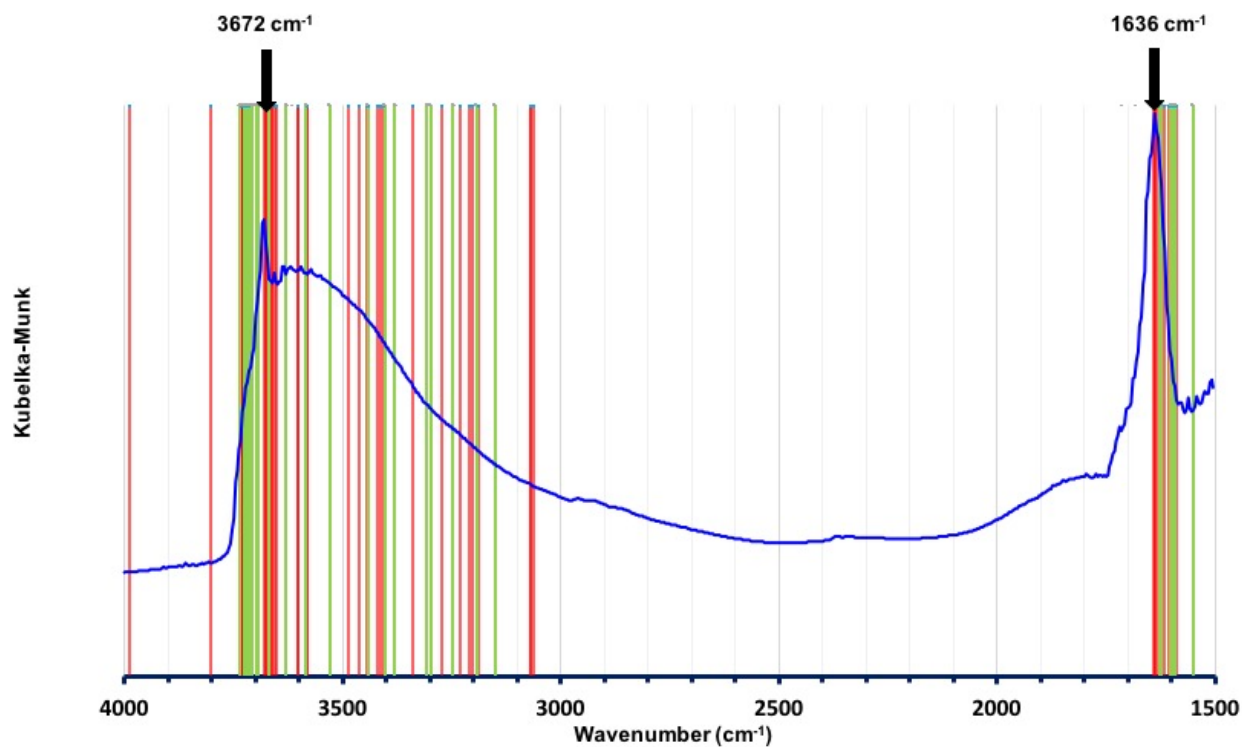
Figure 8a: Comparison of calculated modes of vibration for {130} (red bars) and {100} (green bars) slab models at high water coverage with DRIFTS spectra of MSH com sample taken at 343 K after pretreatment at 343 K. The lines at 3672 cm⁻¹ and 1636 cm⁻¹ (black arrows) appearing on experimental spectra are assigned to structural Mg-OH hydroxyls stretching mode and molecular water adsorbed on Mg ions bending mode respectively. A good match with computed modes is obtained.
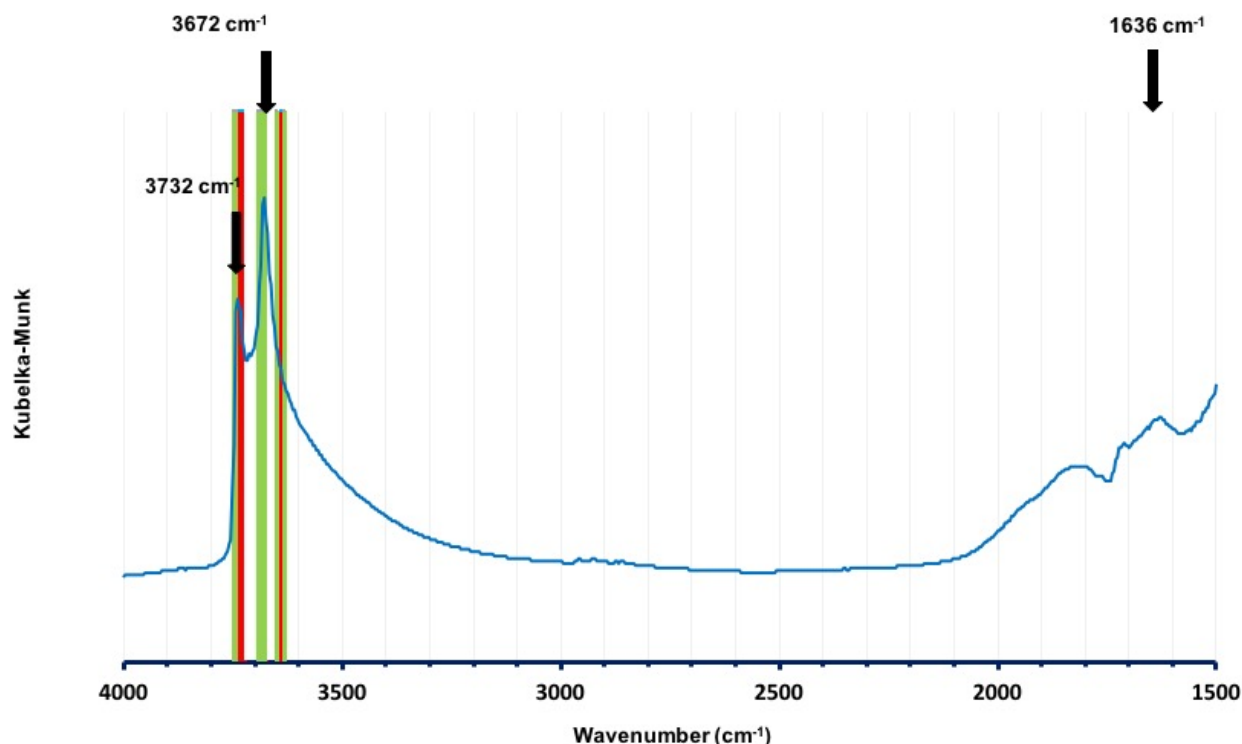
Figure 8b: Comparison of calculated modes of vibration for {130} (red bars) and {100} (green bars) slab models at low water coverage with DRIFTS spectra of MSH com sample taken at 413 K after pretreatment at 623 K under argon flow. The lines at 3732 cm^{-1}, 3672 cm^{-1} and 1636 cm^{-1} (black arrows) appearing on experimental spectra are assigned to edge silanols Si-OH hydroxyls stretching mode, structural Mg-OH hydroxyls stretching mode, and molecular water adsorbed on Mg ions bending mode respectively: the latter, absent from the set of computed modes, has almost disappeared in the experimental spectrum as expected, after high temperature pretreatment under dry flow.

FTIR of adsorbed CO

Transmission FTIR spectra of adsorbed CO provide informations on the character of surface sites through the vibrational Stark effect ([20]). Indeed, shifts of the CO stretching frequency with

respect to the gas phase reference probe the magnitude and orientation of the local electric field at the adsorption sites. The effect arises from the anharmonicity of the potential energy with respect to the C-O bond length. Blue shifts or red shift occur for local fields antiparallel or parallel to the dipole moment vector of CO respectively. We have performed DFT simulations of CO adsorbed on {100} and {130} edge models at low and high coverage by water, on locations A, B and C meaning respectively "above" edge Mg sites (bare at low coverage, above adsorbed water molecules at high overage), "above" edge silanols, and "above" hexagonal windows of basal planes (i.e. nests of structural hydroxyl groups). We note adducts as CO_A(B, C) for adsorption through O, and OC_A(B,C) for adsorption trough C. With our choice of DFT functional and simulation parameters, we obtain 2168.5 cm^{-1} for the harmonic Σ stretching mode of the isolated CO molecule, against 2146 cm^{-1} experimentally (NIST CCCBDB https://cccbdb.nist.gov). Therefore we estimate the anharmonic correction to apply at $-2\omega_e\chi_e = $ -22.5 cm^{-1} very similar to the -27 cm^{-1} whatever the adsorption site reported by Leydier et al. in their recent study of CO adsorption on amorphous-silica models ([23]).

The results of our simulations are summarized in Table 3 and 4, where computed frequencies have been corrected for anharmonicity, and the corresponding minimum energy configurations are presented on Figure S4 to S27 of Supporting Information. These figures reveal, as shown by the shortest CO…HO or OC…HO distance indicated, that on both HC and LC {130} slab models CO_C and OC_C adducts find optimal positions in interaction with a nearby silanol group as well as with the underneath structural Mg$_3$-OH group upon which it was initially positioned. Only LC {100} CO_A and OC_A models end up with adducts unambiguously interacting with bare edge cations at relatively short distances, while their {130} homologs are also in interaction with nearest silanols.

Figure 9 presents the linear correlation obtained between changes of stretching frequencies wavenumbers Δv of CO adsorbed at the various sites relative to gas phase (positive for blue shifts, and negative for red shifts) and the corresponding relative changes of equilibrium C-O bond length $\delta d/d$ (negative if shortened, positive if lengthened). As shown by Leydier et al.[23] for adsorption of CO on amorphous silica-alumina surface sites, the wavenumber shift is proportional to the local electrostatic field experienced by the CO probe in its equilibrium position with respect to the surface, which is the gradient of the local electrostatic potential $\left(\frac{V_O - V_C}{d}\right)$ along the molecule. As reviewed by Fried et al. [20], it is also proportional to the dipole moment change $q\delta d$, assuming no charge transfer between the physisorbed adduct and the substrate. The linear correlations we obtain indicate therefore that $(V_O - V_C)q$ is constant for all these models. With q unperturbed in absence of charge transfer, one must conclude that in the adduct always positions itself with respect to the substrate site in order to experience an approximately constant $(V_O - V_C)$.

Additionally, we notice that absolute wavenumber shifts are correlated to adsorption energies, as shown on Figure S28. As we compute an average adsorption energy for each model involving 2 CO adducts per unit-cell with generally different Δv and $\delta d/d$, we have plotted averages absolute shift in ordinates. Since a significant relative error margin on these weak adsorption energies should be taken into account, we do not obtain an excellent coefficient of correlation, yet the trend is rather clear. This suggests that adsorption energy is mostly stored as elastic energy in the stretched or compressed adduct. As expected the bare edge cation Mg^{2+} is highly or fairly stabilizing CO when adsorbed via the C atom (LC_OC_A for {100}.

Figure 10 compares experimental transmission FTIR spectra of adsorbed CO recorded on MSH com with the predictions of DFT simulations. The spectra were recorded at equilibrium with 1 Torr CO at 77K on samples pretreated under flowing Argon at 343 (HC), and 623K (LC)

respectively. However, predicted wavenumbers for HC and LC are rather well correlated, with the exceptions of OC_A on {100} edge. The experimental spectra differ by their integral area, which might indicate some reduction of surface area at the higher pretreatment temperature, but mostly by the more marked second peak around 2040 cm^{-1} and a non-negligible contribution between 2180 and 2200 cm^{-1}. The former might be explained by components assigned to CO_A, OC_B and OC_C on LC {100} edge. The latter is obviously absent from the set of predicted wavenumbers, therefore not accounted by our models.

In our experiments, the equilibrium adsorption phase was followed by a desorption phase, comprising first an equilibration under static vacuum in presence of a residual CO pressure of circa 0.1 mbar, then the desorption itself under dynamic secondary vacuum. The desorption kinetics were monitored by spectra acquisitions at 0, 2, 4, 6, 10 and 20 min. The evolution of FTIR spectra recorded in the 2100-2200 cm^{-1} is presented on Figures S29 and S30 in Supporting Information. Integral areas decrease exponentially with time as shown on Figure S31, as expected for a desorption kinetics of first order with respect to the residual adsorbed amount of CO. The desorption constants are of the order of 0.1 mn^{-1}, seemingly 50% higher for the sample pretreated at 343K.

We have simulated these spectra as weighted sums of gaussian contributions, of means the predicted wavenumbers, and fixing a constant variance for a given spectrum, assumed to correspond to an instrumental broadening. We allowed the variance and weights to vary along the minimization of objective functions consisting in simple sums of absolute deviations between experimental and simulated absorbances sampled approximately every cm^{-1}. Excellent fits could be obtained with this procedure in the HC case, while in the LC case we had to introduce two extra contributions at initial wavenumbers X = 2185 and Y = 2195 cm^{-1}. Figure S32 a) and S32 b) display

the evolution with desorption time of the weights of the 6 main surviving contributions for the HC and LC cases respectively, obtained following this procedure. We expect the predicted most stable configurations to overweight the others progressively as desorption proceeds in time. This is only partly verified: HC_130_OC_C and LC_130_OC_C have predicted wavenumbers corresponding to the most stable contributions in the experiments, and are indeed predicted among the most stable (see Table 4), but the order of predicted stability is not fully reflected by the orders of survival for the other contributions. However, we note that LC_130_OC_C and LC_100_OC_A contributions go through a maximum at the expense of notably the less stable LC_100_CO_C before 5 mn of desorption time,, which might be indicative of some redistribution in adsorbed phase. Still in the LC case, we notice that if the X contribution at 2185 cm^{-1} decreases slightly and almost linearly with desorption time, the Y contribution at 2195 cm^{-1} appears to increase, suggesting again an evolution of the sample surface state under the desorption conditions applied. Since these lines are not accounted for by our DFT simulations, they should more likely be assigned either to CO or OC adducts outside the nanotalc domains of the MSH samples, or to some defects in the nanotalc phase. CO adducts may interact with silica since the sample bulk and surface have Mg/Si ratios well below the expected stoichiometric value of 0.75 for a TOT magnesium-silicate analogous to talc. As reported by Leydier et al., CO adduct to OH groups in silanol nests at the amorphous silica surface are characterized by a blueshift of 40 cm^{-1} therefore an anharmonic stretching frequency of 2186.5 cm^{-1}, in good agreement with the X contribution we find. However, the latter should also be present on the HC sample. A proper assignation of these X and Y components will require further simulations and experiments.

Table 3: Simulated adsorption of CO probe on {100} slab edge models. HC: high coverage by water; LC: low coverage by water; CO_A: adsorption through O atom at Mg edge site, OC_A: adsorption through C atom at Mg edge site; _B: SiOH edge site; _C: center of hexagonal window in basal plane; ΔE_{ads} : energy of adsorption; ΔG_{ads} : free energy of adsorption of CO at 77 K and 1 Torr; ν_1 : adsorbed CO stretching mode wavenumber, side 1 of the slab (ν_2 : side 2); $\Delta\nu_1$: shift of adsorbed CO stretching mode wavenumber with respect to gas phase CO, numbers in red for red shifts, in blue for blue-shifts ($\Delta\nu_2$: side 2); $d_1(CO)$: C-O bond length, side 1 ($d_2(CO)$: side 2); $\delta d_1/d_1$: relative change of bond length with respect to gas phase CO (computed: 0.11436 nm), ($\delta d_2/d_2$: side 2). ν_1 and ν_2 are reported as computed harmonic mode wavenumbers corrected for anharmonicity by -22 cm^{-1}, the difference between computed gas phase mode (2168.5 cm^{-1}) and experimental (2146.5 cm^{-1} for the unresolved Σ mode).

Adduct	ΔE_{ads}	ΔG_{ads}	ν_1	ν_2	$\Delta\nu_1$	$\Delta\nu_2$	$d_1(CO)$	$d_2(CO)$	$\delta d_1/d_1$	$\delta d_2/d_2$
	kJ.mol^{-1}	kJ.mol^{-1}	cm^{-1}	cm^{-1}	cm^{-1}	cm^{-1}	nm	nm	‰	‰
HC_CO_A	-12.8	+5.3	2134.6	2124.6	-11.9	-21.9	0.11445	0.11455	0.79	1.7
HC_OC_A	-15.1	+1.6	2158.5	2144.5	12.1	-2.0	0.11419	0.1143	-1.5	-0.5
HC_CO_B	-10.2	+4.0	2135.2	2132.2	-11.2	-14.3	0.11448	0.11449	1.05	1.14
HC_OC_B	-17.1	-3.7	2172.0	2168.4	25.5	21.9	0.11405	0.11412	-2.7	-2.1
HC_CO_C	-14.7	-3.1	2163.6	2159.4	17.2	12.9	0.11422	0.11422	-1.2	-1.2
HC_OC_C	-15.2	+5.7	2134.6	2129.2	-11.9	-17.2	0.11441	0.1144	0.44	0.35
LC_CO_A	-17.7	-6.7	2141.9	2138.8	-4.5	-7.7	0.11441	0.11440	0.44	0.35
LC_OC_A	-34.7	-23.3	2173.3	2169.5	26.8	23.0	0.11405	0.11409	-2.7	-2.4
LC_CO_B	-8.0	+3.7	2132.5	2140.3	-13.9	-6.1	0.11448	0.11447	1.05	0.96
LC_OC_B	-16.9	-6.3	2170.4	2167.3	23.9	20.8	0.11407	0.11411	-2.5	-2.2
LC_CO_C	-13.2	-1.3	2160.7	2170.6	14.2	24.1	0.11422	0.11416	-1.2	-1.7
LC_OC_C	-14.3	-2.6	2139.6	2132.2	-6.9	-14.3	0.11452	0.11452	1.4	1.4

Table 4: Simulated adsorption of CO probe on {130} slab edge models. HC: high coverage by water; LC: low coverage by water; CO_A: adsorption through O atom at Mg edge site, OC_A: adsorption through C atom at Mg edge site; _B: SiOH edge site; _C: center of hexagonal window in basal plane; ΔE_{ads} : energy of adsorption; ΔG_{ads} : free energy of adsorption of CO at 77 K and 1 Torr; ν_1 : adsorbed CO stretching mode wavenumber, side 1 of the slab (ν_2 : side 2); $\Delta\nu_1$: shift of adsorbed CO stretching mode wavenumber with respect to gas phase CO, numbers in red for red shifts, in blue for blue-shifts (($\Delta\nu_2$: side 2); $d_1(CO)$: C-O bond length, side 1 ($d_2(CO)$: side 2) ; δ d_1/d_1 : relative change of bond length with respect to gas phase CO (computed: 0.11436 nm), (δ d_2/d_2 : side 2). ν_1 and ν_2 are reported as computed harmonic mode wavenumbers corrected for anharmonicity by -22 cm^{-1}, the difference between computed gas phase mode (2168.5 cm^{-1}) and experimental (2146.5 cm^{-1} for the unresolved Σ mode).

| Adduct	ΔE_{ads}	ΔG_{ads}	ν_1	ν_2	$\Delta\nu_1$	$\Delta\nu_2$	$d_1(CO)$	$d_2(CO)$	$\delta d_1/d_1$	$\delta d_2/d_2$
	kJ.mol^{-1}	kJ.mol^{-1}	cm^{-1}	cm^{-1}	cm^{-1}	cm^{-1}	nm	nm	‰	‰
HC_CO_A	-10.0	-45.6	2138.0	2137.3	-8.5	-9.2	0.11448	0.11454	1.05	0.7
HC_OC_A	-11.1	-45.5	2152.6	2141.9	6.2	-4.5	0.11427	0.11435	-0.79	-0.09
HC_CO_B	-6.9	-40.0	2149.5	2144.1	3.1	-2.3	0.11442	0.11435	0.52	-0.09
HC_OC_B	-7.0	-42.4	2142.5	2135.1	-4.0	-11.4	0.11439	0.11448	0.26	1.05
HC_CO_C	-18.8	-54.4	2133.1	2129.2	-13.4	-17.2	0.11452	0.11454	1.40	1.57
HC_OC_C	-28.3	-59.5	2176.7	2168.5	30.3	22.0	0.11404	0.11407	-2.80	-2.54
LC_CO_A	-10.1	-8.7	2139.6	2137.0	-6.9	-9.5	0.11439	0.11442	0.26	0.52
LC_OC_A	-12.3	-11.0	2150.4	2147.8	4.0	1.4	0.11426	0.11430	-0.87	-0.53
LC_CO_B	-6.4	-3.9	2146.7	2144.4	0.3	-2.1	0.11439	0.11437	0.26	0.09
LC_OC_B	-11.0	-6.2	2162.3	2147.2	15.8	0.8	0.11418	0.11434	-1.57	-0.17
LC_CO_C	-17.6	-16.4	2133.1	2129.4	-13.4	-17.1	0.11452	0.11449	1.40	1.14
LC_OC_C	-24.0	-23.0	2177.3	2172.2	30.8	25.8	0.11403	0.11403	-2.89	-2.89
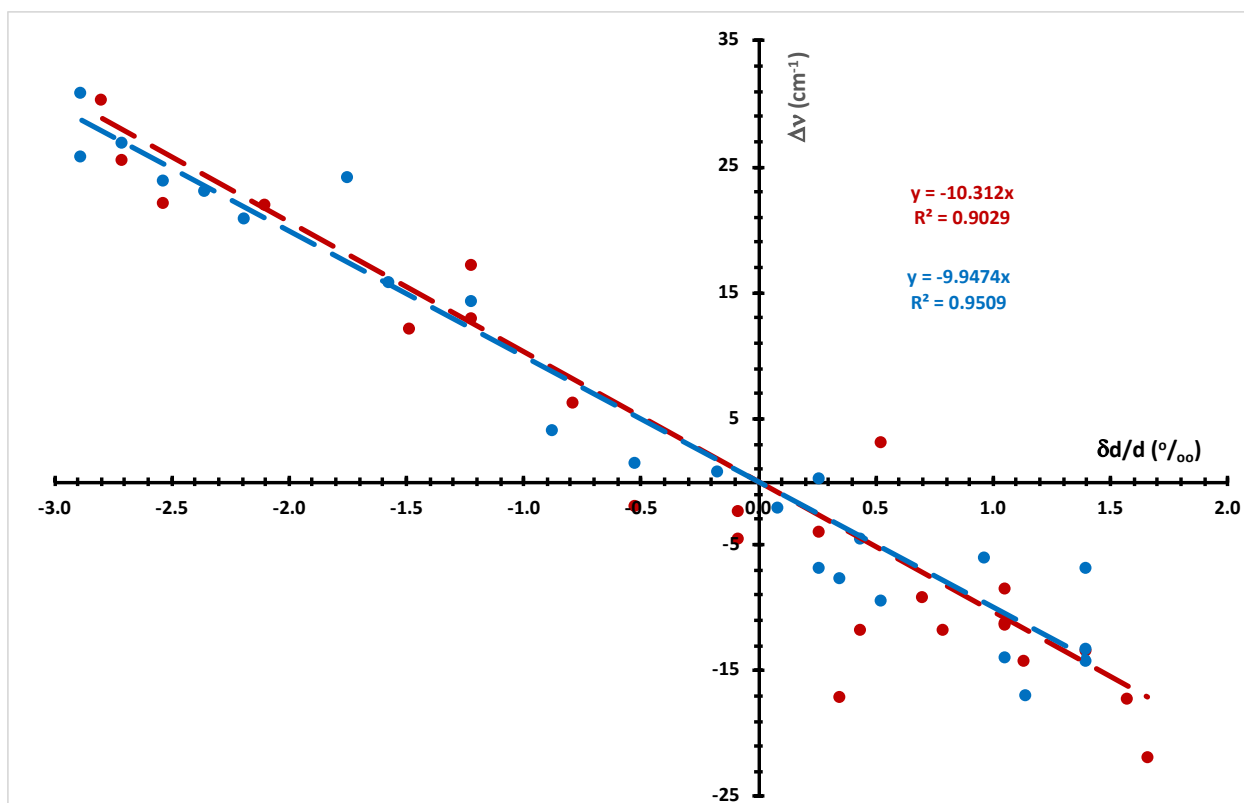
Figure 9: Correlation obtained between changes of simulated stretching frequencies wavenumbers $\Delta\nu$ of CO adsorbed at the various sites relative to gas phase (positive for blue shifts, and negative for red shifts) and the corresponding relative changes of equilibrium C-O bond length $\delta d/d$ (negative if shortened, positive if lengthened). Red dots: HC, Blue dots: LC, {100} and {130} edge slab models. Insets: Equations of regression lines and the corresponding squared coefficients of correlation.
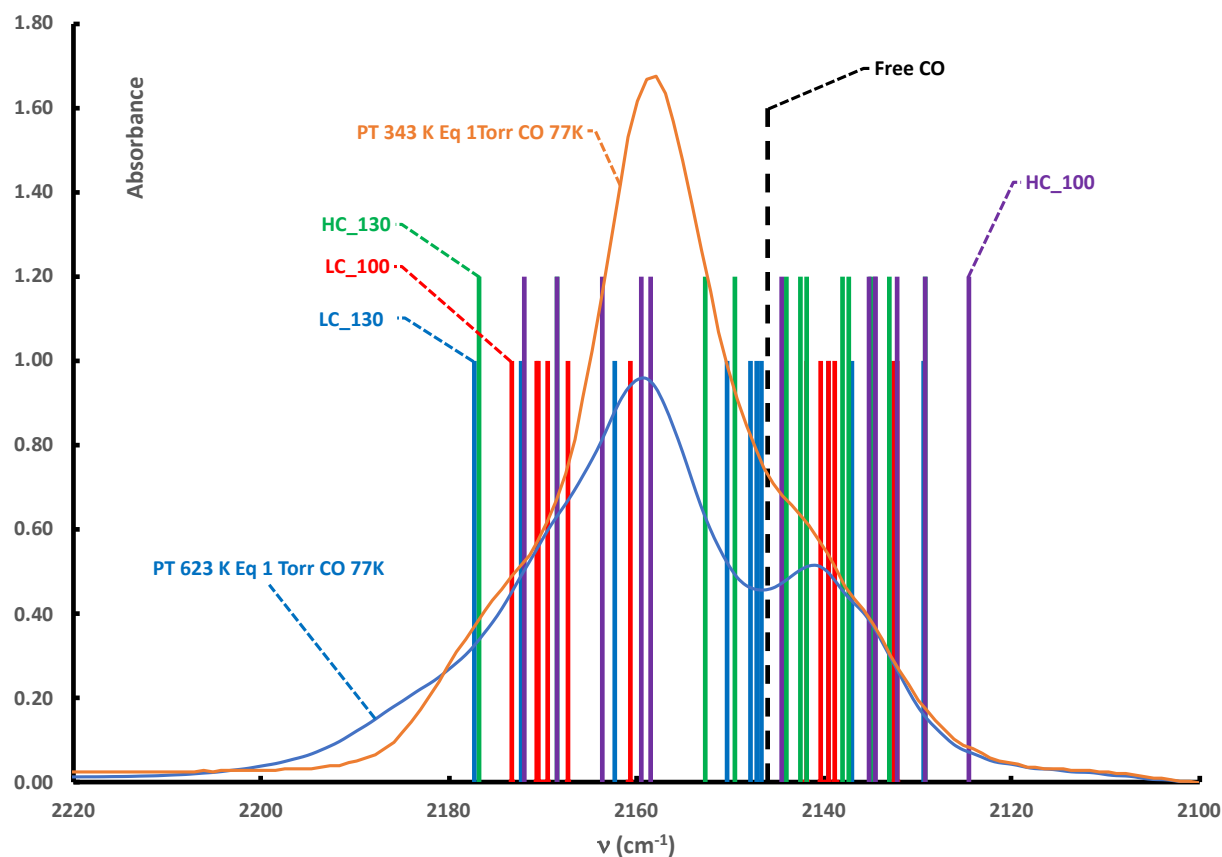
Figure 10: Comparison of experimental transmission FTIR spectra of adsorbed CO recorded on MSH com with the predictions of DFT simulations. The spectra (continuous lines) were recorded at 77K at equilibrium with 1 torr CO. The samples were pretreated under flowing Argon at 343K (orange line) or 623K (blue line), thus predicted to correspond to the high (HC) and low (LC) coverage by water. Simulated stretching frequencies of CO adducts on A, B and C sites of both HC and LC slab models of MSH listed in Table 3 and 4 are superimposed as vertical lines of arbitrary lengths: green HC {130}, violet HC {100}, blue LC {130}, red LC {100}. The stretching frequency of Free CO is indicated as a dotted black vertical line, in order to separate blue shifted from red shifted parts of the spectra.

Comparison of predicted and experimental NMR chemical shifts

Predicted NMR shifts are presented in Table 5.

^{29}Si shifts are compared on Figure 11 to the experimental ^{29}Si DP MAS NMR spectra obtained for our MSH sample and already published ([6]). The models reproduce correctly the contributions expected from Q^3_{SiOMg} in {001} basal planes) and Q^2_{SiOMg} environments of Si, but do not account for contributions observed in the ranges [-70, -81] , [-89, -95], and [-108, -112] ppm. This discrepancy shows that the complexity of MSH cannot be reduced to the Talc structure alone. The Q^4 contribution in the range [-108, -112] ppm is another indication of the presence of amorphous silica together with the CO stretching at 2181 cm^{-1} in the FTIR spectra of adsorbed CO as discussed in the previous section. The contributions in the other ranges will be discussed in depth in a companion paper on nanotalc ([24]).

^{25}Mg shifts are compared on Figure 12 to the already published ^{25}Mg WURST-QCPMG NMR spectrum of MSH com which shows only one peak ([6]). The lineshape simulation with Czjzek model gives an isotropic chemical shift, δiso = 26 ppm and a quadrupolar coupling constant, CQ = 3.5 MHz, in good agreement with Nied et al ([1]). The DFT prediction, average (24 ppm) and range of predicted values (17,3 - 31 ppm) merges all contributions at this scale but corresponds well to the experimental peaks.

^{1}H shifts predictions are compared on Figure 13 to already published ([21]) ^{1}H NMR spectra of MSH com and com-X samples, where X is the temperature of dehydration pretreatment in Kelvin (2h under 20 ml.mn^{-1} Ar flow). The predicted transition between High Coverage (dark and light blue lines for {130} and {100} respectively) to Low Coverage (dark and light red lines for {130} and {100} respectively) by water of TOT magnesium silicate edges as the pretreatment temperature increases, is clearly observed experimentally, in good agreement with DFT

predictions: disappearance of the strong contribution of molecularly chemisorbed water centered around δ ^{1}H = 5 ppm, exaltation of edge Si-OH* contributions around δ ^{1}H = 2 ppm, and shift of the peak assigned to structural Mg$_3$-OH* from δ ^{1}H around 0.3 ppm to δ ^{1}H around 0.8 ppm.

Table 5. Predicted Average Chemicals Shifts in ppm for high coverage (HC) and Low Coverage (LC) by water {130} and {100} Talc Edge Planes Models. Predicted shifts for bulk talc are δ ^{29}Si = -98.0 ± 0.01 ppm, δ ^{1}H = +0.40 ± 0.00 ppm, δ ^{25}Mg = +21.1 ± 0.17 ppm. References for Si and H: TMS, for Mg: MgCl$_2$. Average values are bracketed by average deviations for the various nuclei and situations.

| edge model	{130}HC	{100}HC	{130}LC	{100}LC
δ ^{29}Si bulk (Q^3)	-98.6 ±0.33	-96.4 ±0.49	-100.1 ±0.16	-97.6 ±0.44
δ ^{29}Si edge Si*-OH (Q^2)	-87.4 ±0.22	-85.6 ±1.02	-88.2 ±0.24	-85.9±0.61
δ ^{1}H bulk Mg$_3$-OH*	+0.67 ±0.06	+0.30 ±0.08	+0.91 ±0.07	+1.06±0.31
δ ^{1}H edge Si-OH*	+2.03 ±0.37	+2.02 ±0.46	+2.02 ±0.16	+1.79 ±0.23
δ ^{1}H edge Mg$_2$-OH*	+1.51 ±0.49	+0.82 ±0.30	+1.13 ±0.14	+0.69±0.01
δ ^{1}H edge Mg-OH$_2$*	+4.79 ±1.8	+4.90 ±1.68	-	-
δ ^{25}Mg bulk	+17.7 ±0.37	+19.7 ±0.27	+18.3 ±0.42	+20.4 ±0.79
δ ^{25}Mg edge Mg*-OH$_2$	+16.7 ±1.10	+20.1 ±0.24	+27.7 ±0.42	+30.6 ±0.44
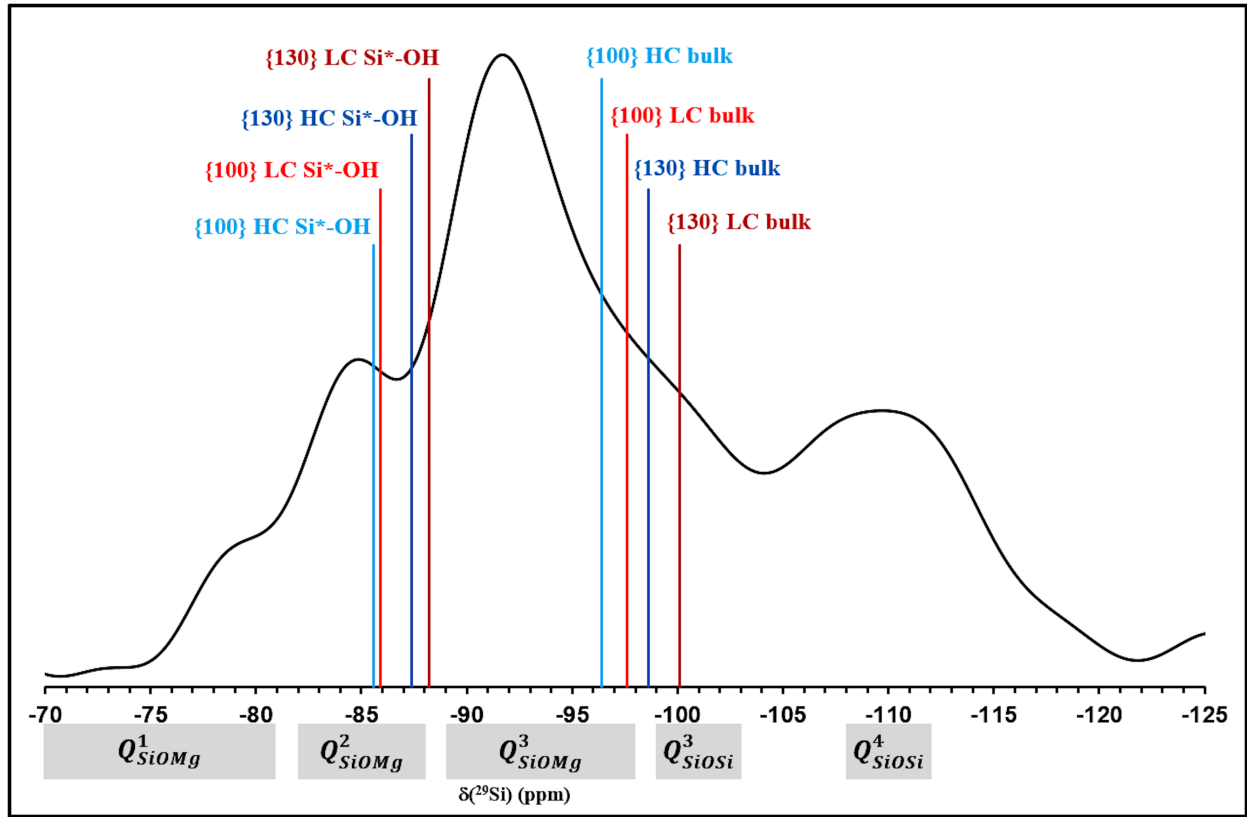
Figure 11: Comparison of experimental ^{29}Si DP MAS NMR spectra of Mg silicate MSH com with predicted average ^{29}Si chemical shifts for {130} and {100} edge models reported in Table 5. Shaded intervals represent the ranges usually assigned in literature according to the labels indicated.
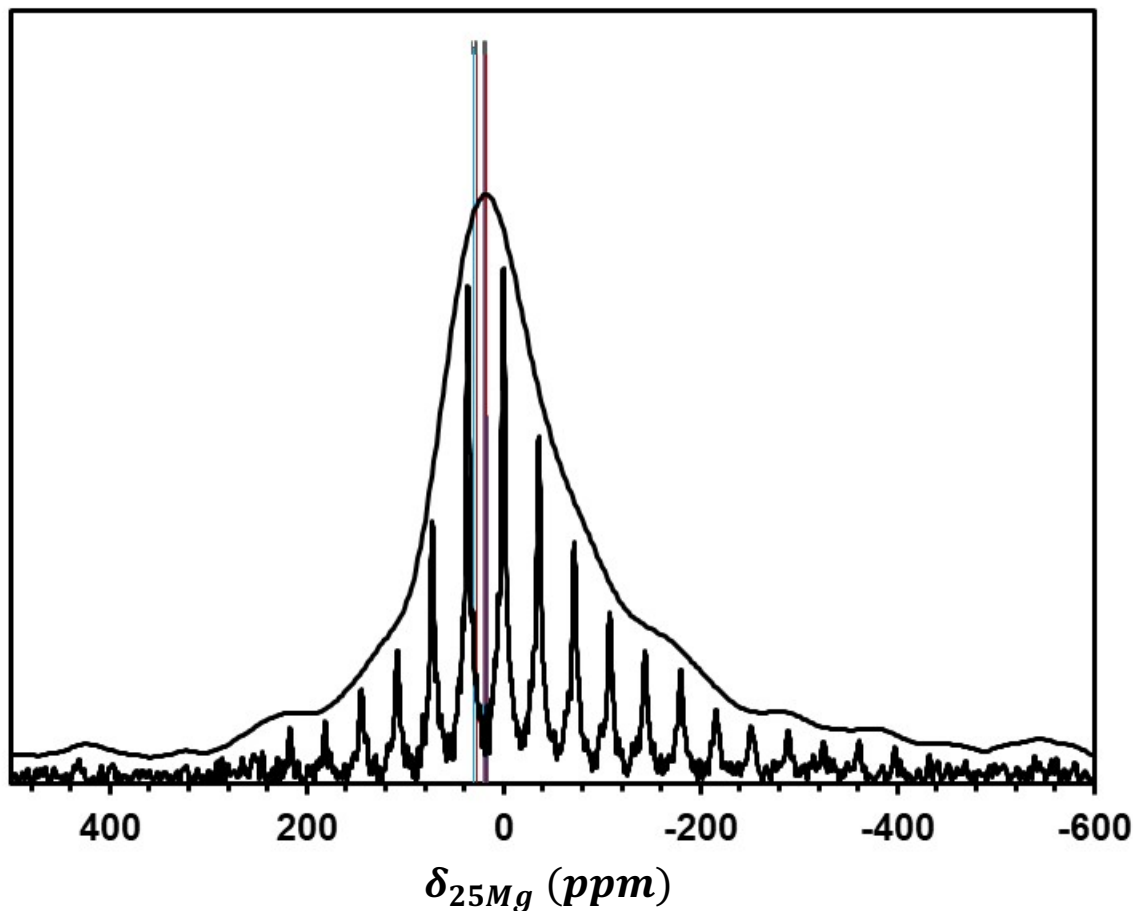
Figure 12: Comparison of experimental [25]Mg WURST-QCPMG NMR spectrum of MSH com with predicted ranges of [25]Mg chemical shifts for {130} and {100} edge models reported in Table 5 (dark and light blue for High Coverage, dark and light red for Low Coverage by water). Experimental spectra, black lines, are composed by spikelet spectrum (bottom) and simulated spectrum according to the Czjzek model (top). The DFT predictions appear merged at this scale but corresponds well to the experimental peaks.
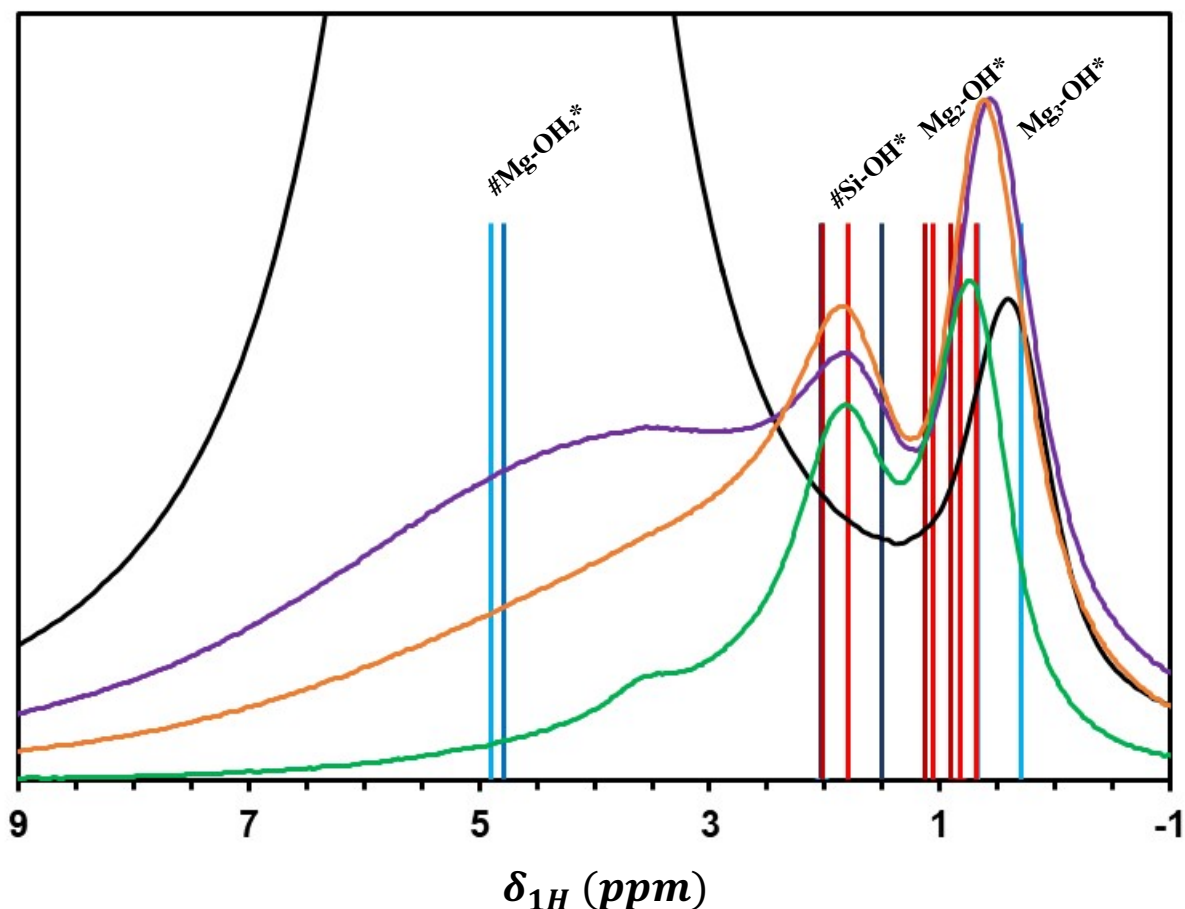
Figure 13: Comparison of predicted (color bars) and experimental (color curves) ^{1}H NMR spectra of MSH com and com-X samples, where X is the temperature of dehydration pretreatment in K (2h under 20 ml.mn[-1] Ar flow). Dark and light blue lines stand for High Coverage {130} and {100} models respectively, and dark and light red lines for Low Coverage {130} and {100} models respectively. The corresponding chemical shifts are listed in Table 5. Black experimental curve: no pretreatment, purple: com-343, orange: com-413, green: com-623

Electron Microscopy

We show in Supporting Information SEM and TEM images (Figures S33 to S36) of the commercial MSH sample: elementary nanoparticles are discernable only at the largest magnification (TEM x100000) as more or less aggregated flat irregular polygons of lateral dimensions 10 nm or less. It is compatible with the predicted morphology, but not conclusive for want of a quantitative image analysis on well separated particles.

Conclusions

We have computed from first principles the surface energies of magnesium-silicate nanoparticles isostructural of talc, modelling the magnesium rich phase of nanosized hydrated magnesium silicates usually denoted as MSH. For that purpose, we have built slab models of oriented dry and hydrated surfaces of talc, and performed DFT geometry optimizations, then normal mode frequencies calculations for these models. The equilibrium morphologies of talc nanoparticles were deduced from these calculations as function of temperature and relative humidity. NMR chemical shifts for ^{1}H, ^{29}Si and ^{25}Mg, and stretching frequencies of CO physisorbed at various sites, were finally computed at the same level of theory for the purpose of comparison with spectroscopic experiments performed on a commercial MSH sample. We report the following conclusions of this work:

Nanotalc equilibrium morphologies express {001}, {130} and {100} families of surfaces in the dry as well as hydrated states, adopting the shapes of flat deformed hexagons. The aspect ratio obtained for the dry state is only slightly affected by dissociative or molecular chemisorption of water on coordinatively unsaturated Si^{4+} and Mg^{2+} surface cations.

The transition from "dry" (D) to "low water coverage" (LC) edge surfaces ({130} and {100}), corresponds to dissociative chemisorption of water by hydrolysis of surface Si-O-Si bridges yielding two surface silanols Si-OH. Dissociative chemisorption energy lies in the [-260, -320] kJ.mol^{-1} range. Predicted stretching modes at 3737 cm^{-1} after anharmonicity correction are consistent with DRIFTS observations.

The transition from "low water coverage" to "high water coverage" (HC) at higher chemical potential of water corresponds to molecular chemisorption of water on coordinatively unsaturated (5-fold) edge Mg^{2+} ions. Molecular chemisorption energies lie in the [-83, -86] kJ.mol^{-1} range. Predicted bending modes of chemisorbed water in the [1600-1700] cm^{-1} range are consistent with DRIFTS observations at circa 1630 cm^{-1}.

From surface thermodynamics diagrams at a given relative humidity, a transition from HC to LC is predicted above the temperature of desorption of molecular water from Mg edge sites. This prediction (515 K) is well matched by the disappearance of the corresponding stretching mode of OH bonds in adsorbed water in experimental FTIR spectra for samples heated at 623 K under dry Ar flow. The predicted transition LC to D state is above 1000K, out of experimental range in our laboratory setup.

Transmission FTIR spectra of CO adsorbed at 77K on MSH com sample are rather well matched by predicted stretching mode wavenumbers of CO physisorbed through C or O sides at edges Si-OH (sites B), edge Mg-H$_2$O and bare edge Mg (sites A), and hexagonal windows of basal planes sites (site C). Blue and red shifts are proportional to relative elongations of C-O bond lengths, indicative of a vibrational Starck effect probing the local gradient of electric field. There are however 2 contributions at high blueshift (2185 and 2195 cm^{-1}) in the LC sample spectrum which are not explained by DFT models.

Predicted ^{1}H NMR spectra assigning chemical shifts in the 6-3 ppm range to protons of chemisorbed molecular water, i.e. sites B, are very well matched with experimental MAS spectra of MSH samples as a broad peak vanishing with increasing pretreatment temperature. Predicted chemical shifts in the 2-1 ppm range assigned to silanol protons, i.e. sites A, are well matched in experimental spectra of MSH by observation of a pretreatment temperature hardly sensitive peak centered on 1.8 ppm. Predicted chemical shifts in the 0.3-0.8 ppm range assigned to the bulk structural hydroxyls (Mg_3-OH), i.e. sites C, are well matched in experimental spectra by a peak centered on 0.5 ppm. Predicted chemical shifts in the 0.8-1.3 ppm range assigned to edge structural hydroxyls (Mg_2-OH) are matched in experimental spectra by a peak centered on 1 ppm.

Increasing chemical shift reflects increased unshielding of protons, thus an increasing Brönsted acidic character for the corresponding sites, thus structural Mg-OH* < edge silanols Si-OH* < edge Mg-OH$_2$*. This order is not systematically followed by the Starck vibrational effects predicted and recorded for CO adducts probing these sites. Therefore, CO adducts frequency shifts do not reflect directly the acido-basic characters of surface sites for nanotalc and the magnesium-silicate nanophase of MSH. It is however correlated to the adduct adsorption energy.

Predicted ^{29}Si NMR spectra assign: i) chemical shifts in the range [-87, -89] ppm to edge Si atoms in Q^2 environment (HO-Si*-(O-Si)$_3$ as observed for MSH samples; ii) chemical shifts in the range [-97, -99] ppm to "bulk" Si atoms in Q^3 environment (MgO-Si*-(O-Si)$_3$ as observed for MSH. The contribution centered around chemical -110 ppm observed for MSH samples is not found in simulations for nanotalc slab models. It is assigned in the literature to Si atoms in Q^4 environment (Si*-(O-Si)$_4$) not present in Talc or nanotalc. This observation for MSH is indicative of the presence of supporting amorphous SiO_2 as suggested by the atomic ratio Si/Mg in excess of

expected 4/3 stoichiometry for nanotalc, and the detection of a CO stretching contribution at 2185 cm^{-1} in FTIR of adsorbed CO experiments.

Predicted ^{25}Mg NMR spectra assign: i) chemical shift in the range [+18, +20] ppm for "bulk" 6-fold coordinated Mg^{2+} ions; ii) similar chemical shift in the range [+17, +20] ppm for "edge" Mg^{2+} ions with completed inner coordination sphere by chemisorbed water molecules; iii) chemical shift in the range [+28, +31] ppm for bare "edge" 5-fold coordinated Mg^{2+} ions, in agreement with the expected deshielding. Experimental isotropic shifts recorded on our MSH samples are in good agreement with predictions. The effect of hydration/dehydration on ^{25}Mg isotropic shifts should be however verified in order to conclude whether the experiment is sensitive enough to detect water desorption from talc-like nanoparticles.

Our prediction of equilibrium morphology could not be directly verified from SEM and TEM image of MSH. It is however tested in more details together with the associated surface speciation, through a multi-technique analysis of synthetic nanotalc samples covering a range of sizes and reported in a companion paper ([24]). On the basis of DFT models, the origin of some features in NMR spectra is interpreted in this paper in terms of structural defects in synthetic nanotalc.

The results of our study confirm the presence of nanosized layered TOT magnesium-silicates similar to nanotalc in MSH. However, both ^{29}Si NMR and adsorbed CO FTIR spectra reveal features absent from those predicted for defect-free nanotalc, which call for further investigations in order to characterize more finely the structure and surface groups in MSH. Defective nanotalc components might prove insightful.

ASSOCIATED CONTENT

Supporting Information.

The following PDF file is available free of charge, containing:

- Correlations between computed shielding constants and experimental chemical shifts for ^{29}Si, ^{25}Mg, and ^1H NMR (Figures S1 to S3).
- Calculated normal modes of vibration obtained for the {130}, {100} slab models of Talc edges at zero, low and high coverage by water (Table S1).
- Geometry optimized conformations of CO adsorbed on Talc edges slab models (Figures S4 to S27).
- Experimental transmission FTIR spectra of CO adsorbed on MSH com (Figures S28 to S32)
- Experimental SEM and TEM imaging of MSH com (Figure S33 to S36)

AUTHOR INFORMATION

Corresponding Author

* herve.toulhoat@orange.fr
+33(0)6 72 76 65 54

Present Addresses

† Present address: School of Chemistry, University of Manchester, Oxford Road, Manchester,

M13 9PL, UK.

Author Contributions

The manuscript was written through contributions of all authors. All authors have given approval

to the final version of the manuscript.

REFERENCES

(1)   Nied, D.; Enemark-Rasmussen, K.; L'Hopital, E.; Skibsted, J.; Lothenbach, B. Properties of Magnesium Silicate Hydrates (M-S-H). *Cem. Concr. Res.* **2016**, *27* (79), 323–332.

(2)   Bernard, E.; Lothenbach, B.; Chlique, C.; Wyrzykowski, M.; Dauzères, A.; Pochard, I.; Cau-Dit-Coumes, Characterization of Magnesium Silicate Hydrate (M-S-H). C. *Cem. Concr. Res.* **2019**, *116* (November 2018), 309–330.

(3)   Claverie, M.; Dumas, A.; Carême, C.; Poirier, M.; LeRoux, C.; Micoud, P.; Martin, F.; Aymonier, C. Synthetic Talc and Talc-Like Structures: Preparation, Features and Applications. *Chem. - A Eur. J.* **2017**, 519–542.

(4)   Dias, G.; Prado, M.; Ligabue, R.; Poirier, M.; Le Roux, C.; Micoud, P.; Martin, F.; Einloft, Pu/Synthetic Talc/Organic Clay Ternary Nanocomposites: Thermal, Mechanical and Morphological Properties. S. *Polym. Polym. Compos.* **2018**, *26* (2), 127.

(5)   Dias, G.; Prado, M.; Ligabue, R.; Poirier, M.; Le Roux, C.; Martin, F.; Fery-Forgues, S.; Einloft, S. Synthetic Talc as a New Platform for Producing Fluorescent Clay Polyurethane Nanocomposites. *Appl. Clay Sci.* **2018**, *158* (November 2017), 37–45.

(6)   Cornu, D.; Lin, L.; Daou, M. M.; Jaber, M.; Krafft, J. M.; Herledan, V.; Laugel, G.; Millot, Y.; Lauron-Pernot, H. Influence of Acid-Base Properties of Mg-Based Catalysts on Transesterification: Role of Magnesium Silicate Hydrate Formation. *Catal. Sci. Technol.* **2017**, *7* (8), 1701–1712.

(7)   Fiorentini, V.; Methfessel, M. Extracting Convergent Surface Energies from Slab

Calculations. *J. Phys Condens. Matter* **1996**, *8*, 6525.

(8) Digne, M.; Sautet, P.; Raybaud, P.; Euzen, P.; Toulhoat, H. Use of DFT to Achieve a Rational Understanding of Acid-Basic Properties of γ-Alumina Surfaces *J. Catal*. **2004**, *226* (1).

(9) Arrouvel, C.; Toulhoat, H.; Breysse, M.; Raybaud, P. Effects of P_{H2O}, P_{H2S}, P_{H2} on the Surface Properties of Anatase-TiO_2 and γ-Al_2O_3: a DFT Study.*J. Catal*. **2004**, *226* (2).

(10) Yates, J. R.; Pickard, C. J.; Mauri, F. Calculation of NMR Chemical Shifts for Extended Systems Using Ultrasoft Pseudopotentials. *Phys. Rev. B* **2007**, *76* (2), 024401.

(11) Gruner, J. W. The Crystal Structures of Talc and Pyrophyllite Locality: Hardford County, Maryland, USA. *Zeitschrift fuer Krist*. **1934**, *88*, 412–419.

(12) Gražulis, S.; Chateigner, D.; Downs, R. T.; Yokochi, A. F. T.; Quirós, M.; Lutterotti, L.; Manakova, E.; Butkus, J.; Moeck, P.; Le Bail, A. Crystallography Open Database – An Open-Access Collection Of Crystal Structures. *J. Appl. Crystallogr*. **2009**, *42* (4), 726–729.

(13) Kresse, G.; Furthmüller, J. Efficient Iterative Schemes for *Ab Initio* Total-Energy Calculations Using a Plane-Wave Basis Set. *Phys. Rev. B* **1996**, *54* (16), 11169–11186.

(14) Perdew, J. P.; Burke, K.; Ernzerhof, M. Generalized Gradient Approximation Made Simple. *Phys. Rev. Lett*. **1996**, *77* (18), 3865–3868.

(15) Grimme, S.; Antony, J.; Ehrlich, S.; Krieg, H. A Consistent and Accurate *Ab Initio* Parametrization of Density Functional Dispersion Correction (DFT-D) for the 94 Elements H-Pu. *J. Chem. Phys*. **2010**, *132* (15), 154104.

(16)   Pickard, C. J.; Mauri, F. All-Electron Magnetic Response with Pseudopotentials: NMR Chemical Shifts *Phys. Rev. B* **2001**, *63* (24), 245101.

(17)   Arrouvel, C.; Digne, M.; Breysse, M.; Toulhoat, H.; Raybaud, P. Effects of Morphology on Surface Hydroxyl Concentration: a DFT Comparison of Anatase-TiO_2 and γ-Alumina Catalytic Supports. *J. Catal.* **2004**, *222* (1).

(18)   Chase, M. W. J. NIST-JANAF Themochemical Tables, Fourth Edition. *J. Phys. Chem. Ref. Data* **1998**, *Monograph*, 1–1951.

(19)   Momma, K.; Izumi, F. VESTA 3 for Three-Dimensional Visualization of Crystal, Volumetric and Morphology Data. *J. Appl. Crystallogr.* **2011**, *44*, 1272–1276.

(20)   Fried, S. D.; Boxer, S. G. Measuring Electric Fields and Noncovalent Interactions Using the Vibrational Stark Effect. *Acc. Chem. Res.* **2015**, *48* (4), 998–1006.

(21)   Lin, L.; Cornu, D.; Mounir Daou, M.; Domingos, C.; Herledan, V.; Krafft, J. M.; Laugel, G.; Millot, Y.; Lauron-Pernot, H. Role of Water on the Activity of Magnesium Silicate for Transesterification Reactions. *ChemCatChem* **2017**, *9* (12), 2399–2407.

(22)   Martins, D. M. S.; Molinari, M.; Mira, J. P.; Parker, S. C. Toward Modeling Clay Mineral Nanoparticles : The Edge Surfaces Of Pyrophyllite And Their Interaction With Water. **2014**.

(23)   Leydier, F.; Chizallet, C.; Costa, D.; Raybaud, P. CO Adsorption on Amorphous Silica–Alumina: Electrostatic or Brønsted Acidity Probe ? *Chem. Commun.* **2012**, *48*, 4076–4078.

(24)   Poirier, M.; Millot, Y.; Silva Gomes, E.; Jaber, M.; Herledan, V.;Laugel, G.; Micoud, P.;

Martin, F.; Lauron-Pernot, H.; Toulhoat, H. Conspiration of Density Functional Theory and Nuclear Magnetic Resonance Tools To Probe the Nano-Layered Silicates Surface Chemistry and Morphology, . Phys. Chem. C **2020**, 124, 1, 267-286**.**

(25)   Schrader, M.E. Spreading Pressure in the Young Equation and Intermolecular Force Theory, *Langmuir* **1993**, 9, 1959-1961.

(26)   Campbell, C. T.; Sprowl, L. H.; Árnadóttir, L. Equilibrium constants and rate constants for adsorbates: Two-dimensional (2D) ideal gas, 2D ideal lattice gas, and ideal hindered translator models, *J. Phys. Chem. C* **2016**, *120,* 10283–10297.

(27)   A. Budi, A.; Stipp, S.L.S.; Andersson, M.P. Calculation of Entropy of Adsorption for Small Molecules on Mineral Surfaces, *J. Phys. Chem. C* **2018**, *122*, 8236–8243.

(28)   Rotenberg, B.; Patel, A.J.; Chandler, D. Molecular Explanation for Why Talc Surfaces Can Be Both Hydrophilic and Hydrophobic, *J. Am. Chem. Soc.* **2011**, *133*, 20521–20527.

TOC Graphic